# *References*


1) Abdel-Salam, T.M., Tiwari, S.N., Chaturvedi, S.K., and Mohieldin, T.O., "Mixing and Combustion in Scramjet Combustor with Raised and Relieved Ramp," AIAA 2000-3709, Presented at the 36th AIAA/ASME/SAE/ASEE Joint Propulsion Conference and Exhibit, July 2000.
2) Arzimovich, Lev A., Elementary Plasma Physics, Blaisdell Publishing Company, New York, pp. 1-7, 1965.
3) Auweter-Kurtz, M. and Rock, W., Spectral Measurements in the Boundary Layer of Probes in Nitrogen/Methane Plasma Flows, AIAA 97-2525, Presented at the 32nd Thermophysics Conference, June 1997.
4) Barbi, E., Mahan, J.R., O'Brien, W.F., and Wagner, T.C., "Operating Characteristics of a Hydrogen-Argon Plasma Torch for Supersonic Combustion Applications," Journal of Propulsion, Vol. 5., No. 2, 1989.
5) Barbi, E., Uncooled Choked Plasma Torch for Ignition and Flameholding in Supersonic Combustion," Masters Thesis, Virginia Polytechnic Institute and State University, 1986.
6) Baev, V.K., Thetjakov, P.K., Dimitrov, V.I., Goloviechev, V.I., and Yasakov, V.A., "Investigation of Gas-Fuel Combustion," CAIM Report, 1977.
7) Baev, V.K., Shumskii, V.V., and Yaroslavtsev, M.I., "Investigation of Gasdynamics of a Model with Combustion in a shock Tunnel," Zhurnal Prikladnoi Mekhaniki I Tekhnicheskoi Fiziki, No. 6, pp. 58-66, November-December, 1983.
8) Barrow, Gordon M., The Structure of Molecules, W.A. Benjamin, Inc., New York, 1963.
9) Baurle, R.A., Gruber, M.R., "A Study of Recessed Cavity Flowfields for Supersonic Combustion Applications," AIAA 98-0938, Presented at the 36th Aerospace Sciences Meeting and Exhibit, January 1998.
10) Baurle, R.A., Tam, C.J., and Dasgupta, S., "Analysis of Unsteady Cavity Flows for Scramjet Applications," AIAA 2000-3617, Presented at the 36th AIAA/ASME/SAE/ASEE Joint Propulsion Conference and Exhibit, July 2000.
11) Beach, H.L., Mackley, E.A., Rogers, R.C., Chinetz, W., "Use of Silane in Scramjet Research," Presented at the 17th JANNAF Combustion Meeting, 1980. CPIA Pub. 329, Vol. I, pp. 639-659.
12) Billig, F.S., "Supersonic Combustion of Storable Liquid Fuels in Mach 3.0 to 5.0 Air Streams," Tenth Symposium (International) on Combustion, The Combustion Institute, Pittsburg, PA, pp.1167-1178, 1965.
13) Billig, F.S., 4th International Symposium on Air Breathing Propulsion, p. 433, 1979
14) Blinder, S. M., Advanced Physical Chemistry: A Survey of Modern Theoretical Principles, The Macmillan Company, London, pp. 86,400-2, 489-96, 1969.
15) Bogdanoff, D.W., "Advanced Injection and Mixing Techniques for Scramjet Combustors," Journal of Propulsion and Power, Vol. 10, No. 2, pp. 183-190, 1994.
16) Bousquet, P., Spectroscopy and its Instrumentation, Adam Hilger Rank Precision Industries, London, 1971.
17) Bowman, C.T., Seery, D.J., "Investigation of NO Formation in Combustion Processes: The Methane-Oxygen-Nitrogen Reaction," Proceedings of the Symposium on Emissions from Continuous Combustion Systems, General Motors Research Laboratories, Plenum Press, New York, 1972.
18) Broadwell, James, "Analysis of the Fluid Mechanics of Secondary Injection for Thrust Vector Control," AIAA Journal, Vol. 1, No. 5, pp. 1067-1074, May 1963.
19) Browning, D.R., Spectroscopy, McGraw-Hill, New York, 1969.
20) Burnes, R., Parr, T.P., and Wilson, K.J., "Investigation of Supersonic Mixing Control Using Cavities: effect of fuel injection location," AIAA 2000-3618, Presented at the 36th AIAA/ASME/SAE/ASEE Joint Propulsion Conference and Exhibit, July 2000.
21) Cambel, Ali Bulent, Plasma Physics and Magnetofluidmechanics, McGraw-Hill Book Company, Inc., New York, 1963.
22) Charton, M., and Gaydon, A.G., *Proc. Phys. Soc*., A, Vol. 69, No. 520, 1958.
23) Chevalier, A., Levin, V., and Bouchez, M., "Frech-Russian Partnership on Hypersonic Wide Ramjets," AIAA 96-4554, 1996.

24) Chrans, L.J., and Collins, D.J., "Stagnation Temperature and Molecular Weight Effects in Jet Interaction," AIAA Journal, Vol. 8, No. 2, pp. 287-293, February 1970.
25) Cobine, J.D., Gaseous Conductors, Theory and Engineering Applications, McGraw-Hill Book Company, Inc., New York, pp. 50, 78-105, 134-7, 167-68, 290-344, 1941.
26) Covault, C., Kandebo, S.W., and Lenorowitz, J.M., "Russian Scramjet Flight Tests," AWST 3/2/92, pp. 18-19, 1992.
27) Cox, S.K., Fuller, R.P., Schetz, J.A., and Walters, R.W., "Vortical Interactions Generated by an Injector Array to Enhance Mixing in Supersonic Flow," AIAA 94-0708, January 1994.
28) Curran, E.T., "Scramjet Engines: The First Forty Years," ISABE 97-7005, 1997.
29) Curran, E.T., "Emerging Propulsion Technologies for the Next Century," AIAA Wright Brothers Lecture, 1999.
30) Davis, D.L., and Bowersox, R.D.W., "Computational Fluid Dynamics Analysis of Cavity Flame Holders for Scramjets," AIAA 97-3270, Presented at the 33rd AIAA/ASME/SAE/ASEE Joint Propulsion Conference and Exhibit, July 1997.
31) Donohue, J.M., McDaniel, Jr., J.C., and Haj-Hariri, H., "Experimental and Numerical Study of Swept Ramp Injection into a Supersonic Flowfield," AIAA Journal, Vol. 32, No. 9, pp.1860-1867, 1994.
32) Drummond, J.P., Carpenter, M.H., Riggins, D.W., and Adams, M.S., "Mixing Enhancement in a Supersonic Combustor," AIAA 89-2794, 1989.
33) Dugger, G. L., "Comparison of Hypersonic Ramjet Engines with Subsonic and Supersonic Combustion," Combustion and Propulsion, Fourth Agard Colloquim, High Mach Number Air-Breathing Engines, A.L. Jaumotte, A.H. Lefebvre, A.M. Rothrock, Editors, Pergamon Press, New York, 1961.
34) Dugger, G.L., and Billig, F.S., "Recent Work in Hypersonic Propulsion at the Applied Physics Laboratory, the Johns Hopkins University," Johns Hopkins University, Applied Physics Laboratory, TG-355, Laurel, MD, November 1959.
35) Ekland, D.R., Stouffer, S.D., and Northam, G.B., "Study of a Supersonic Combustor Employing Swept Ramp Fuel Injectors," AIAA Journal, Vol. 35, pp. 697-704, 1997.
36) Fernando, E.M., and Menon, S., "Mixing Enhancement in Compressible Mixing Layers – An Experimental Study," AIAA 91-1721, 1991.
37) Ferri, A., "Review of Problems in Applications of Supersonic Combustion," J.R. Aeronaut Soc., vol. 68, pp. 575-597. 1964.
38) Ferri, A., "Review of Scramjet Propulsion Technology," J. Aircraft, vol. 5, pp. 3-10, 1968.
39) Finklnberg, W., and Maecker, H., *Electric Arcs and Thermal Plasma*, NASA translation of *Electrische Bogen und Thermishes Plasma*, Handbook of Physics Vol. XXII, Springer-Verlag, Berlin, 1956.
40) Fujimori, T., Murayam, M., Sato, J., Kobayashi, H., and Niioka, T., "Flame-Holding Behind a Wedge by Incident Shock Waves," IUTAM Symposium on Combustion in Supersonic Flows, Kluwer Academic Publishers, pp. 95-100, 1997.
41) Fuller, R.P., Wu, P.K., Nejad, A.S., and Schetz, J.A., "Fuel-vortex Interactions for Enhanced Mixing in Supersonic Flow," AIAA 96-2661, Presented at the 32nd AIAA/ASME/SAE/ASEE Joint Propulsion Conference, July 1996.
42) Gallimore, S.D., "Operation of a High-Pressure Uncooled Plasma Torch with Hydrocarbon Feedstocks," Masters Thesis, Virginia Polytechnic Institute and State University, December 1998.
43) Gaydon, A.G., "The Spectroscopy of Flames," 2nd Ed., John Wiley and Sons, New York, pp. 99-144, 1974.
44) Griem, Hans R., Plasma Spectroscopy, McGraw-Hill Book Company, New York, 1964.
45) Gruber, M., Donbar, J, Jackson, T., Mathur, T., Eklund, D., and Billig, F., "Performance of an Aerodynamic Ramp Fuel Injector in a Scramjet Combustor," AIAA 2000-3708, Presented at the 36th AIAA/ASME/SAE/ASEE Joint Propulsion Conference and Exhibit, July 2000.
46) Gruber, M.R., Nehad, A.S., and Dutton, J.C., "Circular and Elliptical Transverse Injection into a Supersonic Crossflow—The Role of Large-Scale Structures," AIAA 95-2150, Presented at the 26th Fluid Dynamics Conference, June 1995.
47) Hardy, T.L., Electrode Erosion in ARC Discharges at Atmospheric Pressure, AIAA 85-2018, Presented at the 18th International Electric Propulsion Conference, September 1985.

48) Harrison, A.J., and Weinberg, F.J., "Flame Stabilization by Plasma Jets," Proceedings of the Royal Society of London, 321, pp. 95-103, 1971.
49) Harsha, P., and Waldman, B., "The NASP Challenge: Testing for Validation," AIAI 1st NASP Conference, Dayton, OH: July 20-21, 1989.
50) Hodnett, P. F., "Numerically Calculated Properties of a Wall-Stabilized Electric Arc," Journal of Applied Physics, Vol. 40, No. 4, March 15, pp. 1753-1758, 1969.
51) Hollo, S.D., and Hartfield, R., "Quantitative Investigation of Compressible Mixing: Staged Transverse Injection into Mach 2 Flow," AIAA Journal, Vol. 32, No. 3, pp. 528-534, March 1994.
52) Howard, J.C., and Conway, J.G., Nitride and Oxide Bands of Molybdenum, Journal of Chemical Physics, Vol. 43, pg. 3055, 1965.
53) Hoyaux, Max F., Arc Physics, Springer-Verlag New York Inc., New York, 1968.
54) Hsu, K.Y., Carter, C., Crafton, J., Gruber, M., Donbar, J., Mathur, T., Schommer, D., and Terry, W., "Fuel Distribution About a Cavity Flameholder in Supersonic Flow," AIAA 2000-3585, Presented at the 36th AIAA/ASME/SAE/ASEE Joint Propulsion Conference and Exhibit, July 2000.
55) Huebner, L.D., Rock, K.E., Witte, D.W., Ruf, E.G., and Andrews, E.H., "Hyper-X Engine Testing in the NASA Langley 8-foot High Temperature Tunnel," AIAA Paper 2000-3605 AIAA/ASME/SAE/ASEE Joint Propulsion Conference and Exhibit, 36th, Huntsville, AL, July 2000.
56) Jacobsen, L., Schetz, J., and Ng, W., "The Flowfield Near a Multiport Injector Array in a Supersonic Flow," AIAA 98-3126, Presented at the 34th AIAA/ASME/SAE/ASEE Joint Propulsion Conference and Exhibit, July 1998.
57) Jacobsen, L., "An Integrated Aerodynamic-Ramp-Injector/ Plasma-Torch-Igniter for Supersonic Combustion Applications with Hydrocarbon Fuels," Ph.D. Dissertation, Virginia Polytechnic Institute and State University, May 2001.
58) Jacobsen, L., Schetz, J., Gallimore, S., and O'Brien, W., "An Improved Aerodynamic Ramp Injector in Supersonic Flow," AIAA 2001-1766, 10th International Space Planes and Hypersonic Systems and Technologies Conference, April 2001.
59) Jacobsen, L., Schetz, J., Gallimore, S., and O'Brien, W., "Mixing Enhancement by Jet Swirl in a Multiport Injector Array in Supersonic Flow," FEDSM99-7248, Presented at the 3rd ASME/JSME Joint Fluids Engineering Conference, July 1999.
60) Kato, R., and Kimura, I., "Numerical Simulation of Flame-Stabilization and Combustion Promotion by Plasma Jets in Supersonic Air Streams," 26th International Symposium on Combustion, The Combustion Institute, pp. 2941-2947, 1996.
61) Kimura, I., Aoki, H., and Kato, M., "The Use of a Plasma Jet for Flame Stabilization and Promotion of Combustion in Supersonic Air Flows," Combustion and Flame, Vol. 42, pp. 297-305, 1981.
62) Kondratiev, V., and Ziskin, M., *Acta Physiochim*, U.S.S.R., Vol. 7, No. 65, 1937.
63) Kurziner, R.I., "Jet Engines for High Supersonic Flight Velocities," Mashinostroenie, Moscow, 1977.
64) Lawton, J., and Weinberg, F.J., Electrical Aspects of Combustion, Clarendon Press, 1969.
65) Lee, John F., Sears, Francis W. and Turcotte, Donald L., Statistical Thermodynamics, Addison-Wesley Publishing Company, London, pp. 32-3, 63-7, 1963.
66) Lee, M.P., McMillan, B.K., Palmer, J.L., and Hanson, R.K., "Two-Dimensional Imaging of Combustion Phenomena in a Shock Tube Using Planar Laser-Induced Fluorescence," AIAA 91-0460, 1991.
67) Mahan, J.R., "An Experimental Study of the Effects of Local Fluid Constriction on the Confined Discharge Plasma Generator," Ph.D. Dissertation, University of Kentucky, December 1970.
68) Mahan, J.R., Virginia Polytechnic Institute and State University (Blacksburg, VA) Personal Conversation, October 1998.
69) Marble, F.E., Zukowski, E.E., Hendrick, G.J., and Waitz, I.A., AIAA Paper No. 90-1981, 1990.
70) Marr, Geoffrey V., Plasma Spectroscopy, Elsevier Publishing Company, New York, 1968.
71) Masuya, G., and others, Sayama, M., Ohwaki, K., and Kimura, I., "Some Governing Parameters of Plasma Torch Igniter/Flameholder in a Scramjet Combustor," Journal of Propulsion and Power, Vol. 9, No. 2, March 1993.
72) Masuya, G., Chinzei, N. and Miki, Y., "Scramjet Engine Tests at Mach 4 and 6," IUTAM Symposium on Combustion in Supersonic Flows, pp. 147-162, 1997.
73) Masuya, G., Takita, K., Sato, T., and Ohwaki, K., "Ignition of Parallel and Low-Angle Hydrogen Jet by Plasma Torch," 14th ISABE Meeting, September 1999.

74) Masuya, G., Tomoyuki, K., Murakami, A., Shinozaki, N., Nakamura, A., Murayama, M., and Ohwaki, K., "Ignition and Combustion Performance of Scramjet Combustors with Fuel Injection Struts," Jounral of Propulsion and Power, Vol. 11, No. 2, pp. 301-306, March-April 1995
75) Mathur, T., Lin, K.C., Kennedy, P., Gruber, M., Donbar, J., Jackson, T., and Billig, F., "Liquid JP-7 Combustion in a Scramjet Combustor," AIAA 2000-3581, Presented at the 36th AIAA/ASME/SAE/ASEE Joint Propulsion Conference and Exhibit, July 2000.
76) Mathur, T., Streby, G., Gruber, M., Jackson, K., Donbar, J., Donaldson, W., Jackson, T., Smith, C., and Billig, F., "Supersonic Combustion Experiments with a Cavity-Based Fuel Injector," AIAA 99-2102, Presented at the 35th AIAA/ASME/SAE/ASEE Joint Propulsion Conference and Exhibit, June 1999.
77) McClinton, C.R., "Interaction Between Step Fuel Injectors on Opposite Walls in a Supersonic Combustor Model," NASA TP-1174, 1978.
78) McClinton, C., Roudakov, A., Semenov, V., and Kopehenov, V., "Comparative Flow Path Analysis and Design Assessment of an Axisymmetric Hydrogen Fueled Scramjet Flight Test Engine at a Mach Number of 6.5," AIAA 96-4571, November 1996.
79) Miller, G., and Winstead, C., "Emission Profiles of Torch Generated Plasmas," AIAA 96-2304, Presented at the 27th AIAA Plasmadynamics and Lasers Conference, June 1996.
80) Mitani, T., Hiraiwa, Sato, S., Tomioka, S., Kanda, T., Saito, T., Sunami, T., and Tani, K., "Scramjet Engine Testing in Mach 6 Vitiated Air," Presented at the 7th International Space Planes and Hypersonic Systems and Technologies Conference, November 1996.
81) Moore, Walter J., Physical Chemistry, Prentice-Hall, Inc., Englewood Cliffs, NJ, 4th ed., pp. 123, 604-8, 1972.
82) Nickerson, G.R., "Optimized Exhaust Nozzles for Hypersonic Propulsion," AIAA 88-3161, 1988.
83) Northam, G.B. and Anderson, G.Y., "Supersonic Combustion Research at Langley," AIAA Paper No. 86-0159, January 1986.
84) Northam, G.B., Greenberg, I., Byington, C.S., and Capriotti, D.P., "Evaluation of Parallel Injector Configurations for Mach 2 Combustion," Journal of Propulsion and Power, Vol. 8, No. 2, pp. 491-499, March-April 1992.
85) Northam, G.B., McClinton, C.R., Wagner, T.C., and O'Brien, W.F., "Development and Evaluation of a Plasma Jet Flameholder for Scramjets," AIAA 84-1408, Presented at the 20th AIAA/SAE/ASME Joint Propulsion Conference, June 1984.
86) Orrin, J.E., Vince, I.M., and Weinberg, F.J., "A Study of Plasma Jet Ignition Mechanisms," Eighteenth Symposium (International) on Combustion, The Combustion Institute, pp. 1755-1765, 1981.
87) Papoular, R., Electrical Phenomena in Gases, American Elsevier Publishing Company, Inc., London, pp. 123, 138-150, 1963.
88) Payne, M.D., Chrissis, J.W., Pohl, E.A., Bowersox, R.D.W., Gruber, M.R., and Fuller, R.P., "Optimizing Scramjet Fuel Inection Array Design," AIAA 99-2251, Presented at the 35th AIAA/ASME/SAE/ASEE Joint Propulsion Conference, June 1999.
89) Pearse, R.W.B., The Identification of Molecular Spectra," 4th Ed., Chapman and Hall, London, pp. 82-118, 173-176, 217-230, 1976.
90) Perkins, H.D., Thomas, S.D., and Pack W.D., "Mach 5 to 7 RBCC Propulsion System Testing at NASA-LeRC HTF," NASA Technical Memorandum 107384, AIAA 97-0565, Prepared for the 35th Aerospace Sciences Meeting and Exhibit, January 1997.
91) Perrig, Alexandre, "Numerical Model for Plasma Jet Injection in a Supersonic Crossflow," Diploma Work, Swiss Federal Institute of Technology, May 2001
92) Pinkel, I.I., Serafini, J.S., and Gregg, J.L., "Pressure Distribution and Aerodynamic Coefficients Associated with Heat Addition to Supersonic Air Stream Adjacent to Two-Dimensional Supersonic Wing," NACA RM E51K26, February 1952.
93) Rausch, et al., "Hyper-X Program Overview," Presented at the 7th International Spaceplanes and Hypersonic Systems and Technology Conference, Norfolf, VA, AIAA, November 1999.
94) Roudakov, A.S. et al., "Flight Testing an Axisymmetric Ramjet: Recent Russian Advances," IAF Paper No. 93-S.4.485.
95) Roudakov, A., Semenov, V., Kopehenov, V., and Hick, J., "Future Flight Test Plans of an Axisymmetric Hydrogen-Fueled Scramjet Engine on the Hypersonic Flying Laboratory," AIAA 96-4572, Presented at the 7th International Spaceplanes and Hypersonics Conference, November 1996.

96) Roudakov, A.S., Semenov, V.L., and Hicks, J.W., "Recent Flight Test Results of the Joint CAIM-NASA Mach 6.5 Scramjet Flight Program," AIAA 98-1643, Presented at the 8th International Space Planes and Hypersonic Systems and Technologies Conference, 1998.
97) Sabelnikov, V., Walther, R., et al., "Progress in the Joint German-Russian Scramjet Technology Program," ISABE Paper 95-7121.
98) Sakurai, A., "On the Propagation and Structure of the Blast Wave, I," J. Phys. Soc. Japan, Vol. 8, pp. 662-669, 1953.
99) Sands, C.J., Milne, A.M., Clifford, L.J., and Thomas, G.O., "Shock Induced Combustion Over a Rectangular Ramp," IUTAM Symposium on Combustion in Supersonic Flows, Kluwer Academic Publishers, pp. 61-70, 1997.
100) Sato, S., Izumikawa, M., Tomioka, S., and Mitani, T., "Scramjet Engines at Mach 6 Flight Condition," AIAA 97-3021, Presented at the 33rd AIAA/ASME/SAE/ASEE Joint Propulsion Conference and Exhibit, July 1997.
101) Sato, Y., Sayama, M., Katsura, O., Masuya, G., Komuro, T., Kudou, K., Murakami, A., Tani, K., Wakamatsu, Y., Kanda, T., and Chinzei, N., "Effectiveness of Plasma Torches for Ignition and Flameholding in Scramjet," Journal of Propulsion and Power, Vol. 8, No. 4, July 1992.
102) Schetz, J.A., Cox-Stouffer, S., and Fuller, R., "Integrated CFD and Experimental Studies of Complex Injectors in Supersonic Flows," AIAA 98-2780, Presented at the 20th AIAA Advanced Measurement and Ground Testing Technology Conference, June 1998.
103) Schetz, J.A., Virginia Polytechnic Institute and State University (Blacksburg, VA) Personal Conversation, 1999.
104) Schetz, J.A., Weinrub, R., and Mahaffey, R., "Supersonic Transverse Jets in a Supersonic Stream," AIAA Journal, Vol. 6, pp. 933-934, May 1968.
105) Shuzenji, K., Kato, R., and Tachibana, T., "Ignition Characteristics of Arc Discharges Exposed to Supersonic Airflows," AIAA 2000-0617, Presented at the 38th Aerospace Sciences Meeting and Exhibit, January 2000.
106) Smithells, Colin J., Metals Reference Book, 4th Ed., Plenum Press, New York, pp. 52-4, 685-7, 1967.
107) Somerville, J. M., The Electric Arc, John Wiley and Sons, Inc., New York, 1959.
108) Southgate, G.T., Chemical and Metallurgical Engineering, Vol. 31, No. 16, 1924.
109) Spitzer, Lyman Jr., Physics of Fully Ionized Gases, 2nd ed., Interscience Publishers, New York, pp.22-23, 1962.
110) Stouffer, S.D., Baker, N.R., Capriotti, D.P., and Northam, G.B., "Effects of Compression and Expansion-Ramp Fuel Injection Configurations on Scramjet Combustion and Heat Transfer," AIAA 93-0609, Presented at the 31st Aerospace Sciences Meeting, January 1993.
111) Stouffer, S.D., Vandsburger, U., and Northam G.B., "Comparison of Wall Mixing Concepts for Scramjet Combustors," AIAA 94-0587, Presented at the 32nd Aerospace and Sciences Meeting, January 1994.
112) Stouffer, Scott, "Development and Operating Characteristics of an Improved Plasma Torch For Supersonic Combustion Applications," Masters Thesis, Virginia Polytechnic Institute & State University, July 1989.
113) Swithenbank, J., "Hypersonic Airbreathing Propulsion," Program of Aeronautical Science, Vol. 8, pp. 229-294, 1966.
114) Swithenbank, J., Eames, I., Chin, S., Ewan, B., Yang, Z., Cao, J., and Zhao, X., "Turbulent Mixing in Supersonic Combustion Systems," AIAA 89-0260, 1989.
115) Takita, K., Sato, T., Ju, Y., Masuya, G., "Effects of Addition of Radicals Supplied by Plasma Torch on Burning Velocity," AIAA 99-2147, Presented at the 35th AIAA/ASME/SAE/ASEE Joint Propulsion Conference, June 1999.
116) Takita, K., Takatori, F., and Masuya, G., "Effect of Plasma Torch Feedstock on Ignition Characteristics in Supersonic Flow," AIAA 2000-3586, Presented at the 36th Joint Propulsion Conference, July 2000.
117) Takita, K., Uemoto, T., Sato, T., Ju, Y., Masuya, G., and Ohwaki, K., "Ignition Characteristics of Plasma Torch for Hydrogen Jet in an Airstream," Journal of Propulsion and Power, Vol. 36, No. 6, 1999.
118) Tepper, F., and Kaledin, L.A., "Nano Aluminum as a Combustion Accelerant for Kerosene in Air Breathing Systems," AIAA 2001-0521, Presented at the 39th AIAA Aerospace Sciences Meeting and Exhibit, January 2001.

119) Tew, D.E., Waitz, I.A., and Hermanson, J.C., "Streamwise Vorticity Enhanced Mixing Downstream of Lobed Mixers," AIAA Paper No. 95-2746.
120) Thomas, S.R., Perkins, H.D., and Trefny, C.J., "Evaluation of an Ejector Ramjet Based Propulsion System for Air-Breathing Hypersonic Flight," NASA Technical Memorandum 107422, Prepared for the 35th Aerospace Sciences Meeting and Exhibit, January 1997.
121) Tomioka, S., Hiraiwa, T., Sakuranaka, N., Murakami, A., Sato, K., and Matsui, A., "Ignition Strategy in a Model Scramjet," AIAA 96-3240, Presented at the 32nd AIAA/ASME/SAE/ASEE Joint Propulsion Conference, July 1996.
122) Tomioka, S., Jacobsen, S., and Schetz, J.A., "Interaction Between a Supersonic Airstream and a Sonic Jet Injected Through a Diamond-shaped Orifice," AIAA-2000-0088, Presented at the 38th Aerospace Sciences Meeting and Exhibit, January 2000.
123) Trexler, C.A., and Saunders, S.W., "Design and Performance at a Local Mach Number of 6 of an Inlet for an Integrated Scramjet Concept," NASA TN-D-7944, 1977.
124) Tyte, D.C., and Nicholls, R.W., *Identification Atlas of Molecular Spectra*, Vol. 2, University of Western Ontario, 1964.
125) Vinogradev, V., Grachko, V., Petrov, M., and Sheechman, J., "Experimental Investigation of a 2-D Dual Model Scramjet with Hydrogen Fuel at Mach 4-6," AIAA 90-5269, 1990.
126) Viti, Valerio, Contracted work performed at the Aerosoft Company, Blacksburg, VA, 2000.
127) Von Engel, A., Electric Plasmas: Their Nature and Uses, Taylor and Francis Ltd., New York, pp. 80-81, 1983.
128) Wagner, T.C., "Ignition and Flameholding in Supersonic Flow by Injection of Dissociated Hydrogen," Ph.D. Dissertation, Virginia Polytechnic Institute and State University, February 1987.
129) Wagner, T.C., O'Brien, W.F., Northam, G.B., and Eggers, J.M., "Design and Evaluation of a New Injector Configuration for Supersonic Combustion," ISABE 87-7026, 1987.
130) Wagner, T.C., O'Brien, W.F., Northam, G.B., and Eggers, J.M., "Plasma Torch Igniter for Scramjets," Journal of Propulsion, Vol. 5, No. 5, 1989. Originally presented at the 23rd JANNAF Combustion Meeting, 1986.
131) Waltrup, P.J., Billig, F.S., and Stockbridge, R.D., "A Procedure for Optimizing the Design of Scramjet Engines," Journal of Spacecraft and Rockets, Vol. 16, No. 3, pp. 163-172, 1979.
132) Waltrup, P.J., "Liquid-fueled Supersonic Combustion Ramjets: A Research Perspective," Journal of Propulsion and Power, Vol. 3, No.6, pp.515-524, 1987.
133) Waltrup, P.J., Billig, F.S., and Stockbridge, R.D., "Engine Sizing and Integration Requirements for Hypersonic Missile Applications," Symposium on Ramjets and Rockets in Military Applications, AGARD-CP-307, 1982.
134) Waltrup, P.J., et al., "Direct-Connect Tests of Hydrogen-Fueled Supersonic Combustors," 16th Symposium (International) on Combustion, The Combustion Institute, pp. 1619-1630, 1976.
135) Waltrup, P.J., White, M.E., Zarlingo, F., Gravlin, E.S., "History of U.S. Navy Ramjet, Scramjet, and Mixed-Cycle Propulsion Development," AIAA 96-3152, Presented at the 32nd AIAA/ASME/SAE/ASEE Joint Propulsion Conference, July 1996.
136) Warris, A.M., and Weinberg, F.J., "Ignitiona nd Flame Stabilization by Plasma Jets in Fast Gas Streams," Twentieth Symposium of Combustion, The Combustion Institute, pp. 1825-1831, 1984.
137) Weber, R. J. and McKay, J.S., "An Analysis of Ramjet Engines Using Supersonic Combustion," TN 4386, NACA, September 1958.
138) Weinberg, F.J., "Old Flames and New," Inaugural lectures, Imperial College, London, 1968.
139) Weinberg, F.J., Hom, K., Oppenheim, A.K., and Teicham, K., "Ignition by Plasma Jet," Nature, Vol. 272, pp.341-343, 1978.
140) Yatsuyanagi, N., and Chinzei, N., "Status of Scramjet Engine Research at NAL," 20th International Symposium on Space Technology Sciences, ISTS 96-a-2-10, 1996.
141) Yu, K., Wilson, K.J., Smith, R.A., and Schadow, K.C., "Experimental Investigation on Dual-Purpose Cavity in Supersonic Reacting Flows," AIAA 98-0723, Presented at the 36th Aerospace Sciences Meeting and Exhibit, January 1998.

# Appendix A
## A Review of Plasma Spectroscopy

This appendix is meant to serve as an aid to those who are unfamiliar with the fundamentals of spectroscopy, or more specifically, plasma spectroscopy. Interested readers may find further discussions on these subjects in books by Griem (1964), Marr (1968), and Browning (1969). Spectroscopy is a useful method for determining the type and amount of certain molecules or atoms in a specimen where chemical analysis would be difficult. For example, the presence of elements in the sun's atmosphere can be determined using spectroscopic equipment here on Earth, but impossible to evaluate by obtaining an actual chemical sample. Emission spectroscopy is the study of atoms, molecules or ions by the photons they emit. Experiments in the past have indicated that photons behave as both a particle and a wave. Both ideas have validity. This phenomenon of photons has been referred to as the principle of wave-particle duality. It is difficult to visualize light as being both a wave and a particle, since the examples of each in our physical world do not appear to be related. A humorous illustration of this abstract concept is shown in Figure A.1. We can see how, separately, both waves and particles transfer energy in our physical world, but no physical example exists for us to relate to this duality of photons. It is worth noting that, on an empirical level, Einstein's equation $E=h\nu$ links the wave-like properties of a photon to its particle-like properties. E represents the energy of a particle as a function of its frequency, a characteristic of waves. The study of these enigmatic photons is the essence of spectroscopy.

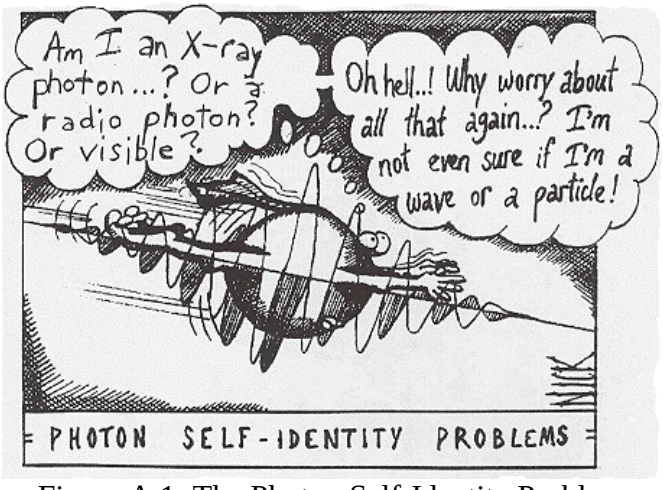

Figure A.1: The Photon Self-Identity Problem

## A.1: Spectroscopy Fundamentals

When someone hears the word "spectrum," they usually think of the visible light spectrum produced by our sun, as seen in Figure A.2. Indeed, most of the work with plasma emission spectroscopy is in the near ultraviolet and visible light regions since these regions contain most of the spectral lines associated with plasma. However, a wealth of information also lies outside these two regions, in the infrared, ultraviolet, radio and x-ray regions. The two most important parameters for spectroscopy are wavelength and intensity. The wavelength of a spectral line, $\lambda$ (measured in nm), is dependent upon the type of molecule or atom being observed, whereas the intensity of a spectral line is related to the concentration of the molecule or atom.

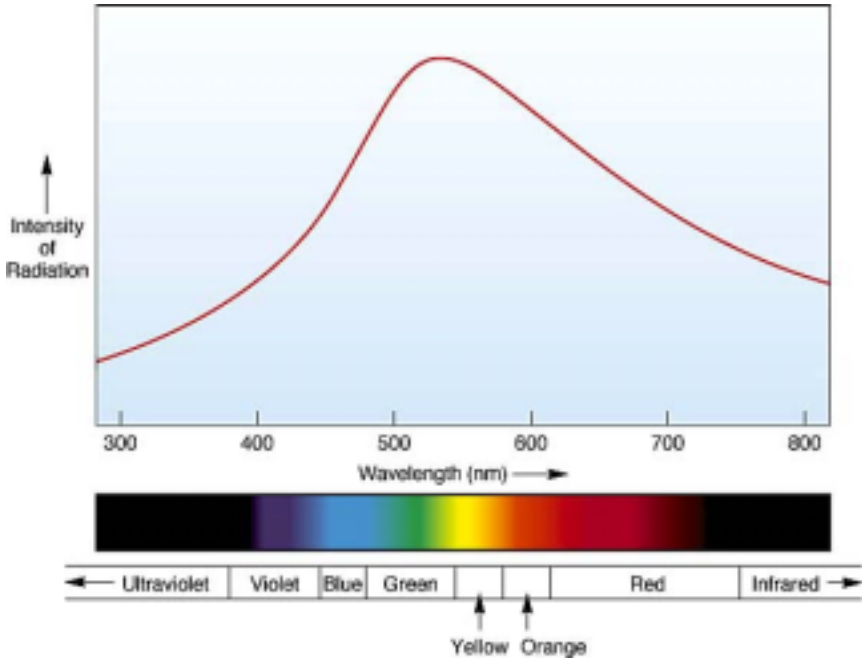


Figure A.2: An Example of the Sun's Spectrum

Spectrometers detect the presence of transient species (atoms, molecules or ions) by the energy they emit in the form of photons. For further information on various spectrographic devices the interested reader can refer to Bousquet (1971). A transient specie, also known as a charged specie, is one in which the electrons of an atom are not in the ground state. The ground state of an atom is that in which the atom has the lowest possible energy (i.e. the electrons occupy all the lowest possible orbital shells). All other

states are referred to as excited states. An example of how photons are emitted can be seen in Figure A.3. Here, a hydrogen atom is shown in its ground state, with its single electron occupying the lowest possible orbital shell. A charged hydrogen atom, shown in Fig A.3b, emits a photon as the electron drops from a higher energy orbital shell to a lower one.

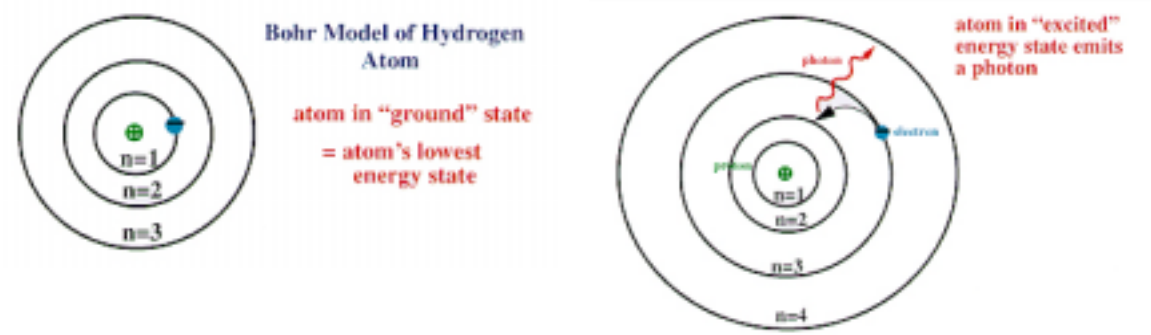


(a) (b)

Figure A.3: An Example of Photon Emission

### A.1.1: Types of Emission Spectra

There are three major types of emission spectra: line spectra, band spectra and continuous spectra. A spectrograph exhibiting examples of all three is shown in Figure A.3. Line and band spectra are sometimes referred to as discontinuous spectra and are unique for each atom and molecule. Charged atoms and atomic ions emitting photons produce line spectra. A spectral line is formed because the electrons can change energy only in fixed amounts, hence producing photons with certain wavelengths. Molecules containing two or more atoms produce band spectra. As with an atom, electrons within a molecule change from one energy level to another, but these changes are also usually accompanied by changes in the vibrational and rotational energies of the individual atoms within the molecule. These changes also cause photons to be emitted, producing a band system consisting of multiple lines where lines from changes in rotational and vibrational energy are superimposed on a spectral line caused by a single electronic transition. At the temperature found within plasma, most molecules are diatomic, and hence, these diatomic molecules make most of the band spectra observed when studying plasma. This concept is further discussed by Barrow (1963). Continuous spectra are produced by

blackbodies, such as the sun, or incandescent light bulbs. A blackbody is a source that distributes its radiated energy among all wavelengths according to the equation

$$I(\lambda,T)=\frac{2\pi hc^2\lambda^{-5}}{e^{hc/\lambda kT}-1}, \qquad \text{(A.1)}$$

where I is the spectral intensity as a function of temperature and wavelength, h is Planck's constant, c is the speed of light and k is Boltzmann's constant. An example of a blackbody curve is shown in Figure A.2.

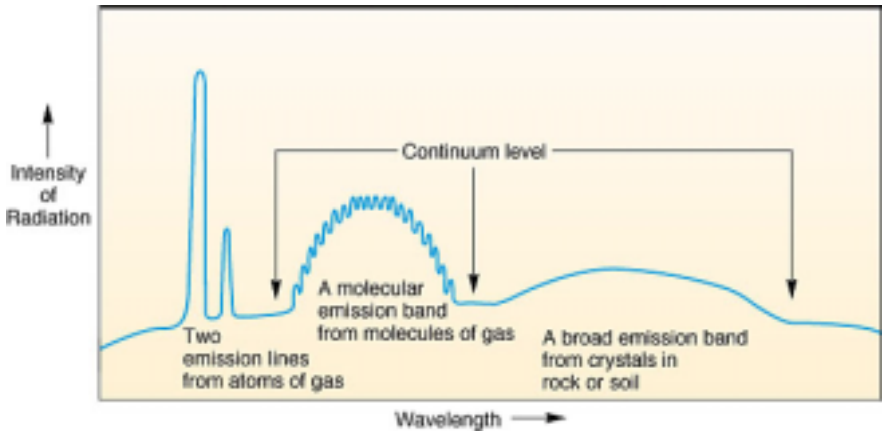


Figure A.4: An Example of Line, Band and Continuous Spectra

**A.1.2: Causes of Spectra**

There are five major causes of molecular spectra. As stated before, when a molecule, or atom, absorbs or emits a photon, its energy is increased or decreased accordingly. These changes in energy most commonly occur through the following five methods: changes in the electron spin resonance, nuclear magnetic resonance, rotational energy levels, vibrational energy levels and electronic energy levels. The first two methods are affected by the presence of a magnetic field, whereas the remaining three can be caused by a multitude of sources. A magnetic field applied to a molecule can affect its electron spin and nuclear spin quantum numbers, S and I respectively. Changes in these two values produce spectra in different regions, but are caused by the same source.

Changes in the vibrational and rotational energy levels of specie are possible only for molecules, since they can store energy by changing the relative velocities between

their individual atoms. Spectra produced by changes in the rotational energy of a molecule occur in the near infrared and microwave regions, while for vibrational energy levels, they occur solely in the near infrared region. The most widely known spectra are those produced by increases or decreases in the electronic energy level of an electron. Electronic spectra occur in the visible and ultraviolet regions of the spectrum.

## A.2: The Prediction of Spectral Lines

By understanding how spectral lines are produced, the spectral signature of a particular sample can be predicted without ever having tested the sample. Early attempts to classify spectral lines used a purely mechanical analogy stating that every spectral line produced by a sample was merely a harmonic or overtone of a fundamental wavelength. This of course is untrue. In 1885, using spectrographic hydrogen data, Balmer created the formula,

$$\lambda = k\frac{n^2}{n^2-4}, \tag{A.2}$$

where $\lambda$ is the wavelength in angstroms, k is a constant and n is an integer, 2, 3, 4, 5, ... This equation accurately predicted the first four hydrogen lines, experimentally discovered by Rowland. These lines are now called the Balmer lines of hydrogen; $H_\alpha$, $H_\beta$, $H_\gamma$, and $H_\delta$ and are represented in Figure A.5. Later experiments showed that the equation did not match so well with other known spectral lines of hydrogen and he modified it to read

$$\frac{1}{\lambda} = R\left(\frac{1}{2^2}-\frac{1}{n_2^2}\right), \tag{A.3}$$

where R is the Rydberg constant. Two other scientists, Ritz and Rydberg, later realized that the value 2 in equation A.3 could have other integer values as well. This led to the discovery of hydrogen lines in the ultraviolet and infrared regions.

In a more general sense, spectral lines of an atom can be predicted if sufficient information is known about the atom's electron energy levels. The energy difference between two levels is directly related to the frequency of the photon emitted when an electron transitions between them. This relationship can be expressed as $h\nu=E_1-E_2$, where $E_1$ and $E_2$ are the corresponding energy levels and $\nu$ is the frequency of the

particle. Naturally, as the atomic number of the atom in question increases, the ability to predict the atom's spectral lines also becomes more difficult.

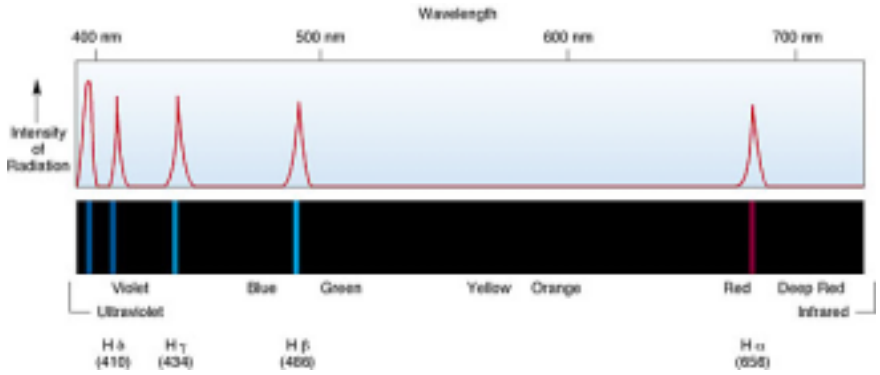


Figure A.5: The Balmer Series for Hydrogen

## A.3: Spectral Line Broadening

Spectral line broadening is the phenomenon by which the natural width of a spectral line is increased, producing a broad, rather than sharp, shape. Three major factors affect the width of a spectral line, Doppler effects, pressure broadening and collision broadening. Since all of these effects are present to some extent, they all contribute to the overall width of a line. The natural line width of a spectral line is determined by the finite amount of time needed for a molecule to change its energy level, whether it is by electronic, vibrational or rotational means.

*Doppler Effects*: The random motions of particles in a gas affect the spectral width of the line and also shift the observed frequency. The relative motion between the particle and the spectrometer causes the shift in frequency. Particles traveling towards the spectrometer will exhibit a blue shift, and those traveling away from the spectrometer, a red shift. Figure A.6 demonstrates this phenomenon. Since the particle motion within a gas is random, this shift will tend to both increase and decrease the observed frequency. The positive and negative frequency shifts will tend to negate each other and a broad line spectrum is observed.

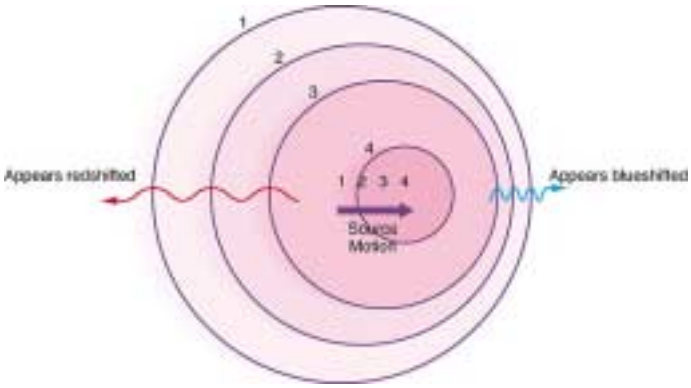


Figure A.6: The Doppler Effect

*Pressure Broadening*: Pressure broadening is caused by intermolecular forces. Forces exerted by surrounding particles can modify the energy levels of a molecule. This type of line broadening is generally valid only for high-pressure gases, liquids and solids.

*Collision Broadening*: Molecules in a gas are continually colliding with one another. These collisions disturb the outer electrons in addition to the rotational and vibrational energy levels of the molecule. This causes a blurring of the spectral line, producing a broader shape. Resonance broadening is similar to collision broadening, but involves only charged species of the same type.

## A.4: Plasma Spectroscopy

In contrast to classical emission spectroscopy, which is used to identify the chemical composition of a luminous source, plasma spectroscopy is also concerned with the properties of the plasma and the nature of the transitions that are not necessarily associated with discrete energy levels. As opposed to gases where collisions dominate the emission or absorption of radiation, the radiation in plasma is largely associated with long-range Coulombic forces between charged particles. Some examples include the broadening of spectral lines through the Stark effect, alterations in the population density of ions and other species, and the emission of continuum. The emission of radiation from self-luminous plasma can be attributed to one of three types of transitions: bound-bound, bound-free and free-free.

Bound-bound transitions refer to electron jumps between discrete energy levels of an atom or molecule. Since the transitions are discrete, the transitions produce distinct line-signatures as determined by the energy difference between the two levels. In an atomic system, these types of transitions produce one or more singlets. Electron transitions within a molecular system are also accompanied by vibrational and rotational transitions, producing a band system. These band systems are also found in flames, as the transitions associated with those systems occur between two discrete energy states as well.

Bound-free transitions are associated with transitions from one ionic state to another and occur only in plasmas and hot flames. The process of recombination (the reverse of photoionization) occurs when an ion and electron recombine, emitting a photon to fall into the next lowest ionization state. Since the upper state is continuous and the lower state is discrete, this type of recombination produces continuous spectra.

Finally, free-free transitions characterize transitions between two free energy levels, that are not discretized, and are associated with the acceleration or deceleration of ions. Generally, these types of transitions are classified as bremsstrahlung or cyclone spectra. Bremsstrahlung spectra are produced through the acceleration of charged particles through the Coulomb field of surrounding charged particles. Since the initial and final states are continuous, the spectra produced by these types of interactions are also continuous. The degree of ionization depends on many different parameters, such as electron density, and temperature, and can significantly affect the appearance of the spectral signature produced by the plasma in that region.

# *Appendix B*
# *Topics Related to Plasma Dynamics*

The purpose of this material is to provide a basic understanding of the plasma state and plasma generators, with an emphasis on plasma heat transfer, to aid in the development of a plasma-injector-ignitor design for use in supersonic combustion applications. Chemical, physical and electrical properties of plasma were studied. The method of plasma generation from electric arcs, and related heat transfer issues, were focused upon in this study. An analysis of the Elenbaas-Heller equation was conducted to better comprehend how plasma properties change with temperature within an electric arc. In addition, a model of arc attachment as a function of gas and arc properties and electrode cooling was developed to determine how changes in a plasma generator, such as current and electrode material, affect the diameter of the arc attachment point on the anode.

## B.1: Plasma as the Fourth State of Matter

A plasma is a gas in which an appreciable number of the molecules are ionized. Plasmas are electrically neutral, consisting of an equal number of positive and negative particles. The term *plasma* first appeared in the early 1920's, introduced by the American physicists Langmuir and Tonks, but the concept of plasma originated in the 1880's when Sir William Crookes reported the odd behavior of low pressure gaseous discharges. He hypothesized that these discharges may be evidence of a new state of matter (Arzimovich, 1965). Despite Crookes' suggestion that a fourth state of matter exists, a large portion of the technical world does not accept this definition, stating that all the properties of plasma (i.e. gaseous matter, electrically conductive, etc.) can be found in the original three (Cambel, 1963).

The majority of stellar matter (>99%) is composed of plasma. Every star is just a large collection of hot, ionized gases. The outer layer of Earth's atmosphere, the ionosphere, also consists of ionized gases produced by solar radiation. Artificially generated plasma is typically produced by means of an electric arc. Unlike stellar plasma, this type of plasma is not in thermal equilibrium because of the localized heating

of the arc and the heat transfer to the cooler surroundings. In addition, on the atomic level, the electrons, ions and neutral atoms all have different mean kinetic energies (Arzimovich, 1965). A plasma is typically thought to have temperatures on the order of 10,000 K and greater. However, in light of the varied kinetic energies of the particles that constitute a plasma, it may be said that a practical plasma consists of a mixture of components at different temperatures. Other definitions have been based on the ionization fraction, charged particle density and chemical properties of the ionized gases being considered. Typically, all of these definitions are related to temperature, which continues to be the leading property cited when defining the plasma state.

## B.2: General Gas Dynamics

The study of this course began with a simple study of gas dynamics, conducted in two parts: physical and energy properties of gaseous particles. The Lennard-Jones potential and theory of collision cross-section describe physical aspects of neutral, gaseous particles interacting with one another. The potential well of an atom, the equipartition of energy principle, and Boltzmann's constant were studied to improve the understanding of the energy characteristics of gaseous particles. These principles were used to learn how gaseous particles interact with one another, how energy affects the electron cloud of an atom, how energy is stored and how energy relates to the absolute temperature of the atom.

### B.2.1: The Lennard-Jones Potential

For any number of atoms in a given volume, there exist both attractive and repulsive forces among them that govern their motion. The repulsive forces are due to the electrostatic repulsion between the electron clouds of adjacent atoms, while the attractive forces are a function of the positions of electrons in one atom relative to those in another. The net repulsive or attractive force is a strong function of distance. An equilibrium position exists between two atoms such that when they are moved closer together, the net force is repulsive, and when they are moved apart, the force is attractive. The variation of interatomic force with distance is commonly referred to as the Lennard-Jones potential, and is described by

$$V_{LJ}(R) = 4\varepsilon\left[\left(\frac{\sigma}{R}\right)^{12} - \left(\frac{\sigma}{R}\right)^{6}\right], \tag{1}$$

where ε is the well depth and σ the separation distance at which V(R) passes through zero. Equation (1) is plotted for a general case in Fig. 2.1.

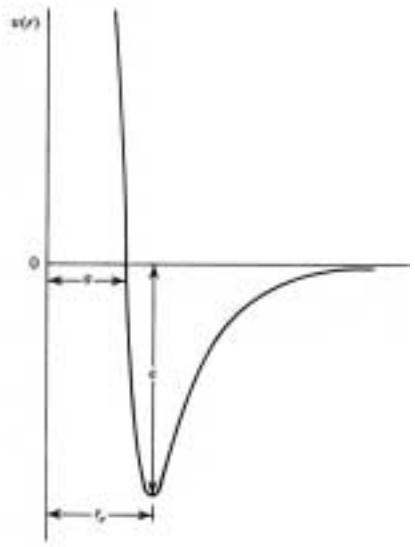

Figure B.1: The Lennard-Jones Potential (Blinder, 1969)

In Figure B.1, $r_e$ is the radius of equilibrium. For atoms at distances greater than $r_e$, an attractive force exists to draw the two atoms back together. As $r \to \infty$, this attractive force approaches zero. A repulsive force exists for atoms at distance less than $r_e$. This repulsive force approaches infinity as the intermolecular separation approaches zero. The actual force of attraction or repulsion between two atoms can be calculated from the potential energy function V(R), by means of $F=-dV/dr$ (i.e. the slope of the curve). It is clear from Fig. 2.1 that the force (slope of the function) between two atoms is zero at the bottom of the well and at $r \to \infty$, and infinity as $r \to 0$. Each type of atom or molecule will have a different potential curve depending on its chemical properties (i.e. different values of ε and σ). Figure B.2 shows the Lennard-Jones potential for several different atoms and molecules.

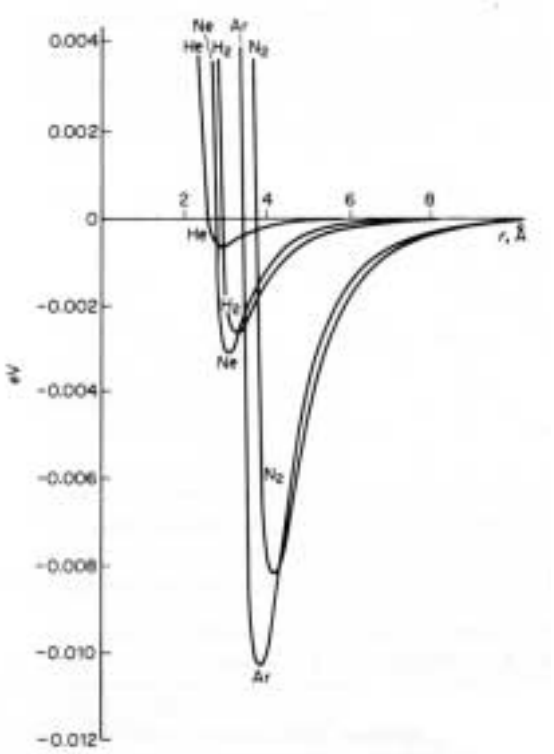


Figure B.2: Lennard-Jones Potentials for Several Molecules (Moore, 1972)

**B.2.2: The Theory of Collision Cross-Section**

Molecules in a liquid or gaseous state undergo many collisions with other molecules as they travel within their volumetric boundaries. The effective collision cross-sectional area between two molecules is defined as

$$\sigma = 4\pi r^2 . \tag{2}$$

Note that $\sigma$ in Eq. (2) is not the same quantity as in the Lennard-Jones potential, Eq. (1) A graphical interpretation of Eq. (2) is given in Fig. 2.3. A collision is said to have occurred between two molecules when their centers (or nuclei) have come within two radii of each other, effectively carving out a circle of area $4\pi r^2$.

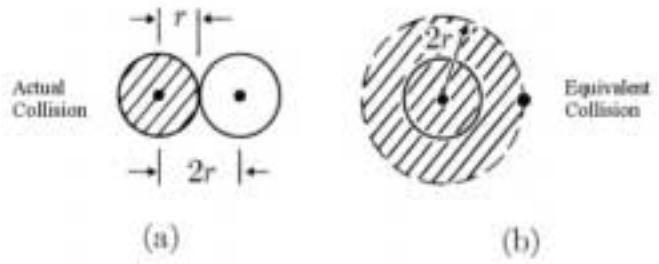


Figure B.3: Representation of Collision Cross-section (Lee et al., 1963)

For n molecules per unit volume, a molecule traveling with an average speed of $\bar{v}$ is expected to experience an average of $\sigma n \bar{v} t$ collisions for a length of time, t. This is simply the volume swept out by a molecule with a collision cross-section of σ, multiplied by the number of molecules in that volume. The average distance between collisions (free path), assuming all particles are moving with a Maxwellian velocity distribution, is

$$\lambda = \frac{1}{\sqrt{2}} \frac{1}{\sigma n}. \tag{3}$$

Equations (2) and (3) are valid for a molecule traveling among other stationary molecules with the same radius. For an electron traveling among molecules of gas Eq. (3) becomes

$$\lambda_e = 4 \frac{1}{\sigma n}. \tag{4}$$

This difference is due to the much smaller radius of an electron when compared to a molecule.

**B.2.3: The "Potential Well" of an Atom**

The Schr $\bar{d}$inger equation provides the basis for understanding quantum mechanics. The simplest application of the Schr $\bar{d}$inger equation is the concept of a "particle in a box." For a particle moving in one dimension, let's say along the x-axis, and with impenetrable limits at x = 0 and x = a, there exist quantum levels at which the particle may be found depending on its energy level. The limits at "0" and "a" form a boundary that gives rise to the name "potential well." Avoiding a long and involved derivation, the allowed energy levels for the particle are

$$E_n = \frac{h}{8ma^2} n^2, \qquad \text{n = 1, 2, 3,…} \tag{5}$$

where h is Planck's constant. Figure B.4 shows a graphic representation of the potential well for a particle in a wire. From the figure and Eq. (5), it is apparent that subsequent energy levels are simply a multiple from the lowest energy level $E_1$. This level is commonly referred to as the ground state. It is interesting to note that for this quantum mechanical model $E_1>0$, whereas for a classical mechanical model the ground state would have a kinetic energy equal to zero. Therefore, it is impossible to reduce the

kinetic energy of an atomic particle to zero, a condition that does not exist in classical mechanics.

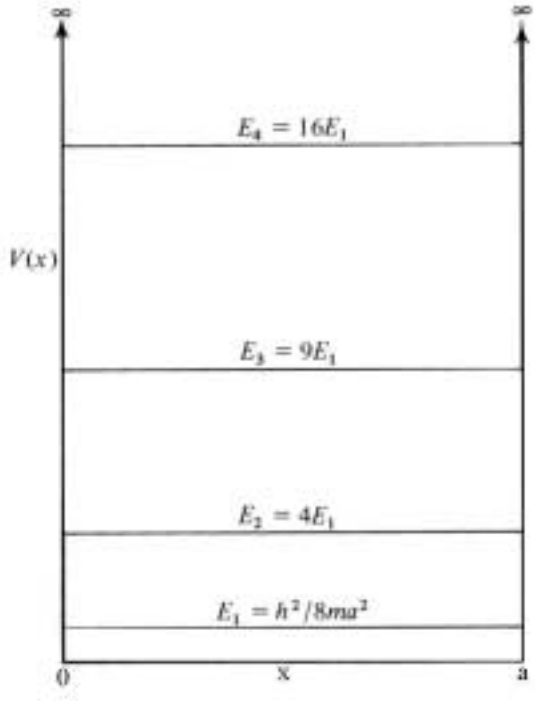


Figure B.4: The Potential Well and Allowable Energy Levels for a Particle on a Wire (Blinder, 1969)

**B.2.4: Equipartition of Energy Principle**

The classical equipartition of energy principle states that, on average, the total energy absorbed by a molecule is partitioned equally among the three modes of motion within a molecule, namely, translational, rotational and vibrational (Blinder, 1969). These modes of energy storage are defined as follows:

Translational: Motion of the center of mass of the molecule, maintaining the geometry and three-dimensional orientation of the molecule.

Rotational: Motion of the nuclei about the center of mass of the molecule without changing the internuclear separation of the atoms.

Vibrational: Motion of the nuclei that involves change in the internuclear separation of the atoms, but not the center of mass.

Examples of these modes are shown in Fig. 2.5 for a diatomic molecule. A molecule is said to have 3n degrees of freedom, where n is the number of atoms present in the molecule. The center of mass of the molecule has three degrees of translational motion regardless of the number of atoms present. Consequently, there are 3n-6 vibrational degrees of freedom for nonlinear molecules and 3n-5 for linear ones, leaving the remaining degrees of freedom to the rotational mode.

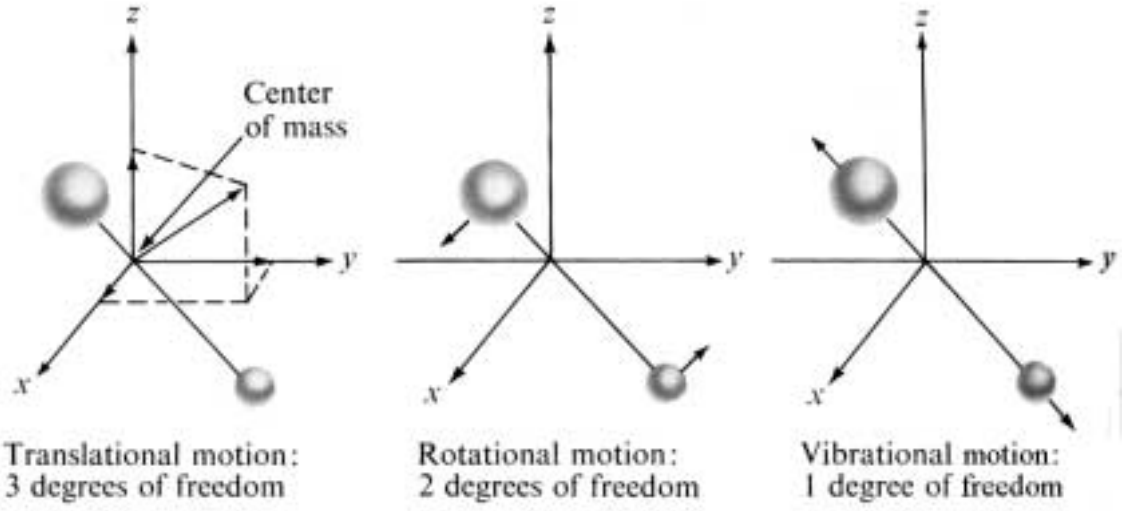


Figure B.5: Nuclear Motions for a Diatomic Molecule (Blinder, 1969)

The theorem is based on classical quantum mechanics, in which the application to translational motion and room temperature rotational motion agrees with quantum mechanics. The theory predicts the storage of ½ RT of energy per mole for each translational or rotational degree of freedom and RT per mole for each vibrational mode, in the molecule upon heating. However, the vibrational mode is highly quantized and depends strongly on temperature. As an example, as the mass of the molecule increases, the vibrational frequency decreases, yielding a greater contribution to the heat capacity. For simple molecules the equipartition principle predicts heat capacities close to the experimental value, but for more complex molecules, it cannot account for the large discrepancy caused by the vibrational modes of energy storage (Moore, 1972). Table 2.1 demonstrates this distinction.

**Table B.1: Heat Capacities of Gases at 278 K (Blinder, 1969)**

| Molecule | $C_v/R$ (experimental) | $C_v/R$ (equipartition) |
|---|---|---|
| He | 1.50 | 1.5 |
| Ne | 1.50 | 1.5 |
| $H_2$ | 2.47 | 3.5 |
| $N_2$ | 2.50 | 3.5 |
| $O_2$ | 3.15 | 3.5 |
| $I_2$ | 3.43 | 3.5 |
| $CO_2$ | 3.47 | 6.5 |
| $NH_3$ | 3.29 | 9.0 |
| $C_2H_6$ | 5.33 | 21.0 |

In conclusion, the equipartition principle is a general tool used to predict the energy storage methods and calculate the specific heat of atoms and molecules.

### B.2.5: Boltzmann's Constant

James Clerk Maxwell first worked out a method for determining the distribution of molecular velocities in 1859. Ludwig Boltzmann later refined Maxwell's method using statistical mechanics. This research yielded much in determining the most commonly used equation of state for an ideal gas,

$$pV = N\frac{R}{N_o}T\,, \tag{6}$$

where $N_o$ is Avogadro's Number and R is the universal gas constant. The ratio $R/N_o$ is commonly referred to as Boltzmann's constant and given the symbol k. Boltzmann's constant is defined as

$$k = \frac{R}{N_o} = \frac{8.3144x10^3(J/kg\cdot mole\cdot K)}{2.0251x10^{26}(molecules/kg\cdot mole)} = 1.3803x10^{-23}(J/molecule\cdot K) \tag{7}$$

The equation of state for an ideal gas can then be rewritten

$$pV = kNT\,, \tag{8}$$

which is generally the more familiar form. By rearranging and replacing some terms in this equation with aspects of molecular theory, the equation of state can finally be written

$$\frac{1}{2}m\bar{v}^2 = \frac{3}{2}kT\,. \tag{9}$$

Equation (9) gives a molecular interpretation of the mean translational kinetic energy of the molecule in terms of its absolute temperature. One important aspect of this relation is that the mean translational kinetic energy is solely a function of the absolute temperature. In other words, for the same absolute temperature, $H_2$, He, $O_2$, Ne, $N_2$, etc. would all have the same mean translational kinetic energy despite the large differences in mass (Lee et al., 1963). Also, for mixtures not in thermal equilibrium the mean translational kinetic energy of the electrons would be much greater than that of the ions or neutral particles, because of their higher absolute temperature.

In addition, the mean total energy of a molecule with n degrees of freedom can be shown to be $\bar{\varepsilon} = \frac{n}{2}kT$. With the specific internal energy per mole being $u = \frac{n}{2}RT$ and $c_v = \left(\frac{\partial u}{\partial T}\right)_v$ it can be shown that $c_v = \frac{n}{2}R$, or in terms of Boltzmann's Constant, $c_v = \frac{n}{2}N_o k$.

## B.3: Plasma Dynamics

For this section, the study of plasma dynamics was separated into three parts. First, the interaction of charged particles with one another is discussed with regard to ambipolar diffusion. The concept of shielding demonstrates how charged particles interact with electrically insulated walls and electrical fields. Finally, the measurement of the density of charged particles is discussed with the description of the Langmuir probe.

### B.3.1: Ambipolar Diffusion

The diffusion of both positive and negative particles takes place in charged gases. This diffusion creates an electric field. Also, the particles with opposite polarity are coupled together so that they tend to move with a common velocity, $V_a = V^+ = V_e$. This coupling is especially strong in charged gases with a high concentration of positive and negative particles, as in an atmospheric-pressure electric arc (Von Engel, 1983).

Figure B.6(a), represents a contained, uniformly distributed collection of positive ions and electrons. Once the barrier is removed diffusion of both positive ions and

electrons takes place. However, because the electrons have a higher diffusion coefficient they tend to disperse more quickly, leaving a net positive charge at the origin and creating a net negative charge at the outer edges just after the barrier is removed, as indicated in Figure B.6(b). This difference in charge tends to drag the positive ions away from the origin and slow the escape of the electrons at the out edges until a common velocity is reached between the two types of particles. Ideally all particles are dispersing with the same velocity after the initial starting transient. This phenomenon is known as *ambipolar diffusion*. The ambipolar diffusion coefficient, $D_a$, depends on the mean electron energy $kT_e$ and the nature of the gas. A measure of how quickly the charged gas will disperse, its value is

$$D_a = \frac{kT_e}{e}\mu^+, \tag{10}$$

where $\mu^+$ is a measure of the positive ion mobility.

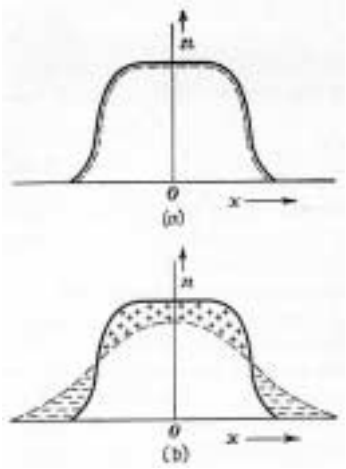


Figure B.6: Ambipolar Diffusion, Ion and Electron Densities
(a) Initially
(b) After a small time increment
(Cobine, 1941)

**B.3.2: Shielding**

The process of shielding electrically insulated walls from plasma occurs naturally by means of an electric field and may go against the initial intuitive notion that some sort of physical barrier is formed, which the term shielding seems to imply. When an

insulating wall is first exposed to plasma it is electrically neutral. Due to the high initial velocity of the electrons and relatively low velocity of the positive ions, higher numbers of electrons impact the insulating wall than ions. This causes the insulating wall to acquire a negative charge, repelling electrons and attracting positive ions until the flux of each into the wall is equal (Popoular, 1963). The wall develops a negative potential relative to the plasma given by

$$V_D = -\frac{kT_e}{2e}\ln\left(\frac{T_e}{T_i}\frac{m^+}{m^-}\right). \tag{11}$$

This process is known as *shielding*.

Due to the negative charge of the wall, positive ions build up in close proximity to the wall, but the concentration of electrons near the wall is practically zero. This region is commonly referred to as a *Debye sheath* and forms whenever plasma comes in contact with a solid surface. The thickness of the Debye sheath is

$$\lambda_D = \left(\frac{kT}{4\pi n_e e^2}\right)^{\frac{1}{2}} \approx 6.90\left(\frac{T}{n_e}\right)^{\frac{1}{2}}, \tag{12}$$

where $\lambda_D$ is measured in centimeters, $n_e$ is the concentration of electrons per cubic centimeter and T is the temperature of the plasma in kelvins. Without this sheath the plasma would lose electrons much more rapidly than ions because of the higher velocity of electrons (Spitzer, 1962). The shielding distance is typically larger than the average distance between charged particles. However, higher concentrations of charged particles require a stronger electric field to isolate the charges from the wall. In order to accomplish this, the Debye sheath thickness must decrease.

### B.3.3: The Langmuir Probe

One of the earliest methods used to measure the density of charged particles in a plasma was to insert an insulated probe into the plasma and measure the potential taken on by the probe. Langmuir, however, decided to implement an uninsulated probe consisting of a thin wire that protrudes from a sealed thin glass tube. A Langmuir probe is used to measure the absolute positive ion density of a charged gas. The concept behind the probe is very similar to that of shielding. Langmuir would insert the probe into a

region of plasma and vary its potential with relation to one of the electrodes. He would then measure the probe current as a function of its potential. As the probe is made increasingly more negative, fewer electrons will impact the probe tip and a region of positive ions will form around the surface of the probe, creating a sheath. The positive-ion current passing through the probe is proportional to the ion density of the plasma. Additionally, it has been shown that

$$i_p \propto V^{\frac{3}{2}}\left(1+0.0247\sqrt{\frac{T}{V}}\right), \tag{13}$$

where V is the potential across the positive-ion sheath and T is the absolute temperature of the ions at the plasma side of the sheath (Cobine, 1941).

## B.4: Arc Analysis

With a general understanding of gas and plasma dynamics, a study of arc analysis was conducted with the focus on plasma generation. This investigation centered primarily on free-burning arcs. The Steenbeck entropy minimum principle was investigated as way of relating electric arc variables and entropy production in an electric arc. In addition, the Elenbaas-Heller equation was used to construct temperature profiles of an arc with both constant and variable parameters relating gas properties to temperature. Finally, a model of the arc attachment point on the anode was created to relate the arc attachment point diameter to various gas and electrode properties.

### B.4.1: Free-Burning Arcs

An arc is defined as a self-sustaining discharge having a low voltage drop and the ability to support large amounts of current density, typically in the range of several tens of thousands of amperes per square centimeter on the electrodes (Papoular, 1963). They are typically characterized as having an extremely bright core surrounded by an aureole. Figure B.7 shows the relationship of an arc to other types of electric phenomena, such as glow discharges. Arcs can be classified as either free-burning or constricted. A constricted arc is one that passes from a cathode, through some constricting channel, to an anode. A free-burning arc has no such restriction and is typically generated between two pointed electrodes, one pointed electrode and a flat plate or two spheres.

Constriction is a means of stabilizing an arc and confining it to an area in which it can produce useful effects.

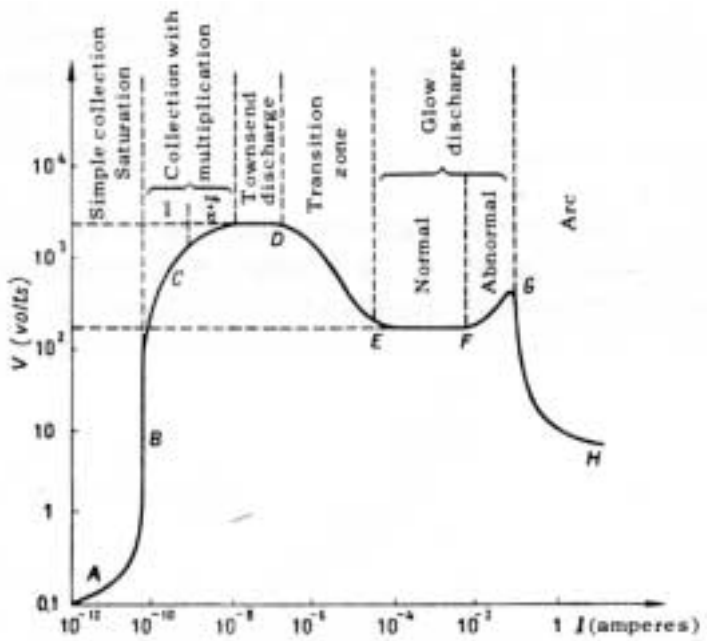


Figure B.7: Schematic Characteristic for Gaseous Discharges (Papoular, 1963)

Another reason for constricting an arc is to increase the temperature of the arc core. Free-burning arcs are generally at atmospheric pressure and the gas temperature is usually 5000 K or above. Figure B.8 shows the difference between the electron and gas temperatures of high-pressure and low-pressure arcs. At high pressures (about 200 mm Hg and above), the temperature of the ions, electrons and neutral particles in the positive column are all in thermal equilibrium. The same is not true for low-pressure arcs, where the electron temperature can reach as high as 40,000 K (Cobine, 1941).

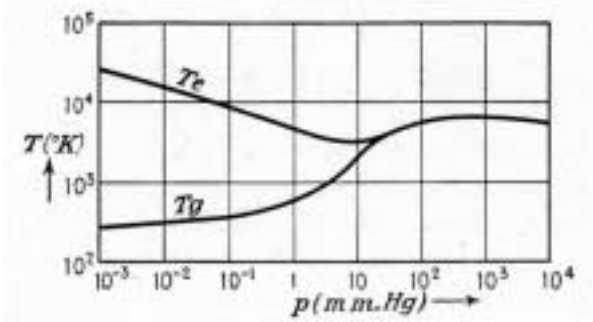


Figure B.8: Dependence of Gas and Electron Temperature on Pressure (Cobine, 1941)

The length of an arc is made up of three regions; the cathode and anode fall regions and the positive column. These three regions are shown graphically in Figure B.9. The cathode fall region ($V_c$) is only about 0.001 mm thick depending on the pressure of the gas. The electric field strength in this area is very strong. Only electrons are found in this region, so no plasma is present. The current density is highest in this section of the arc because the arc is narrowest at the cathode. The length of an arc largely falls within the description of a positive column. In contrast to the cathode fall region, the electric field strength is much weaker, but constant, in the positive column. This region is considered electrically neutral so it is classified as a plasma. The anode fall region ($V_a$) has a strong electric field and contains only electrons, much like the cathode fall region. However, the anode fall region is thicker than the cathode fall region by several orders of magnitude.

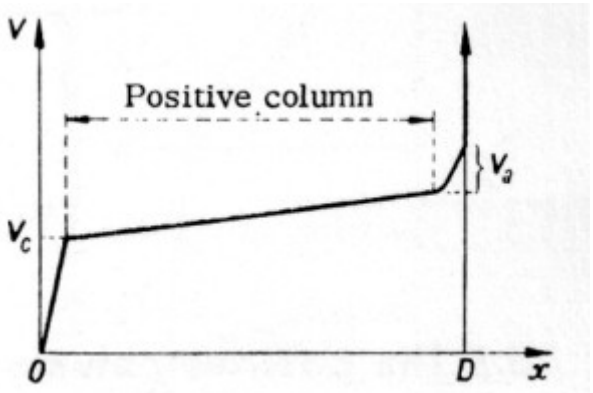


Figure B.9: The Regions of an Arc (Cobine, 1941)

**B.4.2: Entropy Production in an Electric Arc**

For an arc with a fixed length and current, the primary dependent arc variable is the current density, which is related to the arc conductivity and arc diameter, which in turn is related to the electric field strength. For high-pressure arcs, the arc diameter and electric field strength are related by the Steenbeck minimum principle that states that the independent variables of an electric arc will be adjusted so that the rate of entropy production is minimized (Finklnberg and Maecker, 1956). The entropy production per unit length, Θ, with considerations from irreversible thermodynamics is

$$\Theta = \frac{IE}{T_c}, \tag{14}$$

where $T_c$ is the temperature of the arc core, E is the electric field strength and I is the total current passing through the arc. The integral of this quantity along the length of the arc is the total entropy production in the arc. According to the Steenbeck minimum principle, if current is uniform, the electric field strength must be minimized in order to minimize entropy production. Steenbeck's minimum principle may be tentatively stated as follows: "Each time an electrical discharge phenomenon seems to have a choice between more than one configuration, it tends to achieve that implying the minimum voltage drop," (Hoyaux, 1968). In other words, the tradeoff between the diameter of the arc and the electric field is such that entropy production is minimized.

### B.4.3: The Elenbaas-Heller Equation

The Elenbaas-Heller energy equation is used to describe a fully-developed arc in which all of the local power input is lost to the constrictor walls through radiation and conduction. The Elenbaas-Heller energy equation is

$$\frac{1}{r}\frac{d}{dr}\left[rk(T)\frac{dT}{dr}\right] = \lambda(T) - \sigma(T)E^2, \qquad (15)$$

where k(T) is the thermal conductivity, $\lambda$(T) is the radiation energy loss per unit volume, $\sigma$(T) is the electrical conductivity and E is the magnitude of the electric field (Hodnett, 1969).

Two analyses were done based on the Elenbaas-Heller equation. The objective was to determine the radial temperature distribution of a constricted argon arc in the positive column and to ascertain how the variables k, $\sigma$ and $\lambda$ affect the results. For the first, and simplest, of the two analyses, k, $\sigma$ and $\lambda$ were all assumed constant, independent of temperature. A wall temperature of 300 K and dT/dr=0 at the center of the constrictor were the two boundary conditions. Fig. 4.4 shows the normalized results of that calculation. The second analysis used k(T), $\sigma$(T) and $\lambda$(T) for ionized argon as described by Hodnett and tabulated in Table B.2. For the second analysis, plasma was assumed to exist only above 5100 K.

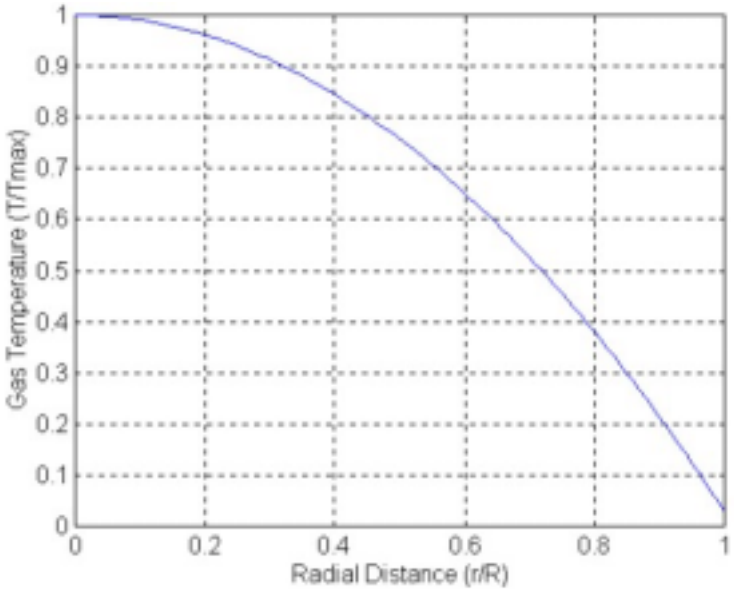


Figure B.10: Temperature Distribution of an Argon Arc with Constant k, σ and λ

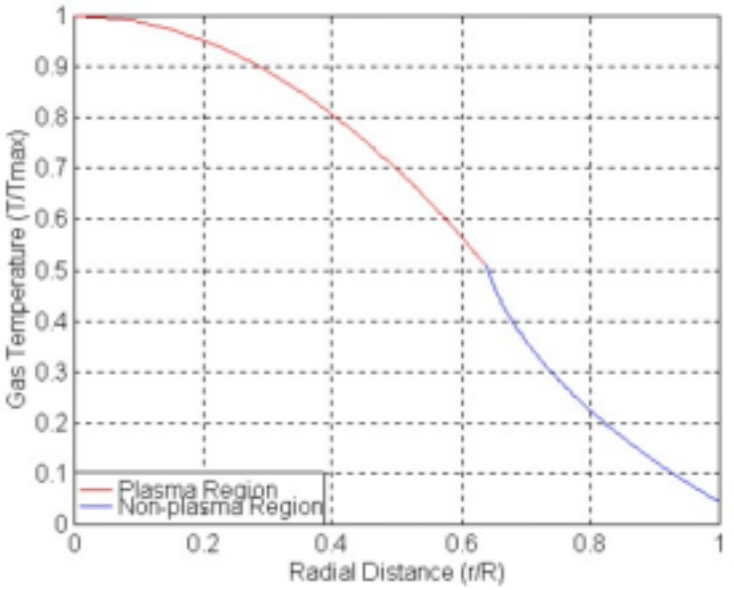


Figure B.11: Temperature Distribution of an Argon Arc with k(T), σ(T) and λ(T) (given by Table B.2)

It is clear from Figures B.10 and B.11 that the use of constant gas properties k, σ and λ is really not a bad assumption, providing that the properties are calculated at a temperature which produces roughly the same $T_{max}$. The use of gas properties dependent upon temperature seems to change the calculated temperature profile very little. One slight change occurred when using temperature-dependent gas properties as opposed to constant gas properties. The former calculation assumes the edge of the plasma region behaves as a

constant temperature wall, producing a small "kink" in the temperature profile, whereas for the constant properties case the boundary condition is at the constrictor wall. However, the conclusion remains the same, that the use of constant values for gas properties in the Elenbaas-Heller equation is a good assumption for producing representative temperature profiles of the positive arc column in a cylindrical tube. In the future, an improved model should include three temperature regions to smooth out the temperature profile. Recommended ranges are: $T_{max} \rightarrow$ 6000 K, 6000 K$\rightarrow$ 4000 K and 4000 K $\rightarrow T_{wall}$.

Table B.2: Gas Properties for Ionized Argon

| Properties for weakly ionized argon | Properties for strongly ionized argon |
|---|---|
| $K(T) = 1.0051\times10^{2}T^{\frac{1}{2}} ergs/\deg\cdot cm\cdot s$ | $K(T) = 0.3859\times10^{-5}T^{\frac{5}{2}} ergs/\deg\cdot cm\cdot s$ |
| $\lambda(T) = 0$ | $\lambda(T) = 1.18512\times10^{10}\left[(T-4000)/12800\right]^{4.795} ergs/cm^{3}\cdot s$ |
| $\sigma(T) = 0$ | $\sigma(T) = 0.48098\times10^{10}(T-4000) esu$ |

**B.4.4: Anode Attachment Point Model**

A second study was performed to determine how various arc parameters and plasma properties affect the area of arc attachment on the anode. The following equations were used:

$$\dot{S}_s = \dot{Q}_a\left(\frac{1}{T_a}-\frac{1}{T_p}\right), \tag{16}$$

$$\dot{Q}_a = I\phi_a + \xi IV_{af} + \pi\frac{d_a^{\,2}}{4}\left[h\left(T_p - T_a\right) + k_e\frac{\left(T_p - T_a\right)}{\delta} + \sigma\varepsilon\left(T_p^{\,4} - T_a^{\,4}\right)\right], \tag{17}$$

$$\dot{Q}_a = k_a\pi\frac{d_a^{\,2}}{4}\left(\frac{T_a - T_c}{t}\right), \tag{18}$$

and

$$\frac{\partial\dot{S}}{\partial d_a} = 0, \tag{19}$$

where

| | | |
|---|---|---|
| | I=100 | Current |
| | Tc=298 | Temperature of coolant (K) |
| | $\phi_a$=4.38 | Thermionic work function of copper (V) |
| | $\varepsilon$=1.0 | A multiplication factor ($0\le\varepsilon\le1$) |

| | |
|---|---|
| $\xi$=1.0 | A multiplication factor ($0 \le \xi \le 1$) |
| $V_{af}$=20 | Voltage across anode fall region (Mahan, 1970) |
| h=125 | Heat transfer coefficient (W/mK) |
| $T_p$=10000 | Temperature of plasma (K) |
| $k_e$=399.0 | Conductivity of electrons in the anode fall region (W/mK) |
| $\delta$=0.001 | Thickness of anode fall region (m) |
| $\sigma$=5.67E-8 | Boltzmann's constant ($W/m^2K^4$) |
| $k_a$=320.0 | Conductivity of copper at melting temp (W/mK) |
| t=0.001 | Thickness of anode (m) |

were used as initial values to begin the study. For this analysis, $k_e$ was assumed to be the conductivity of copper at room temperature. Solving for $d_a$ as a function of all other parameters allowed the dependency of $d_a$ on t, $\delta$, I, $V_{af}$, $k_e$ and $\phi_a$ to be evaluated. It was found that the diameter of the arc attachment point decreases exponentially with increases in the anode thickness and thermal conductivity of the electrons in the anode fall region. Increasing the current and thermionic work function of the electrode caused a linear increase in the arc diameter at the point of attachment. These trends are shown in Figure B.12.

These trends can be explained using logical electrical arguments and knowledge of arc physics. In Figure B.12(a), a thicker anode is expected to have a smaller arc attachment point. As the anode thickness increases, so does its thermal resistance, given by

$$R_{thermal} = \frac{t}{k_a}. \tag{20}$$

A larger thermal resistance will produce a higher local temperature on the anode surface, $T_a$. To minimize the heat transfer to the anode, the arc diameter must decrease according to equation (18), which also agrees with the previous statement. In Figure B.12(b), shows that an increase in the thermal conductivity of the electrons in the anode fall region produces a decrease in arc attachment diameter. According to the Lorentz ratio,

$$L = \frac{\sigma_e}{k_e}, \tag{21}$$

as the thermal conductivity of an electron gas increases, the electrical conductivity must also increase to maintain a constant ratio. It is also known that as the electrical

conductivity of an electron gas increases, the charge concentration must increase (i.e. in the case of an electric arc, the arc constricts) (Papoular, 1963).

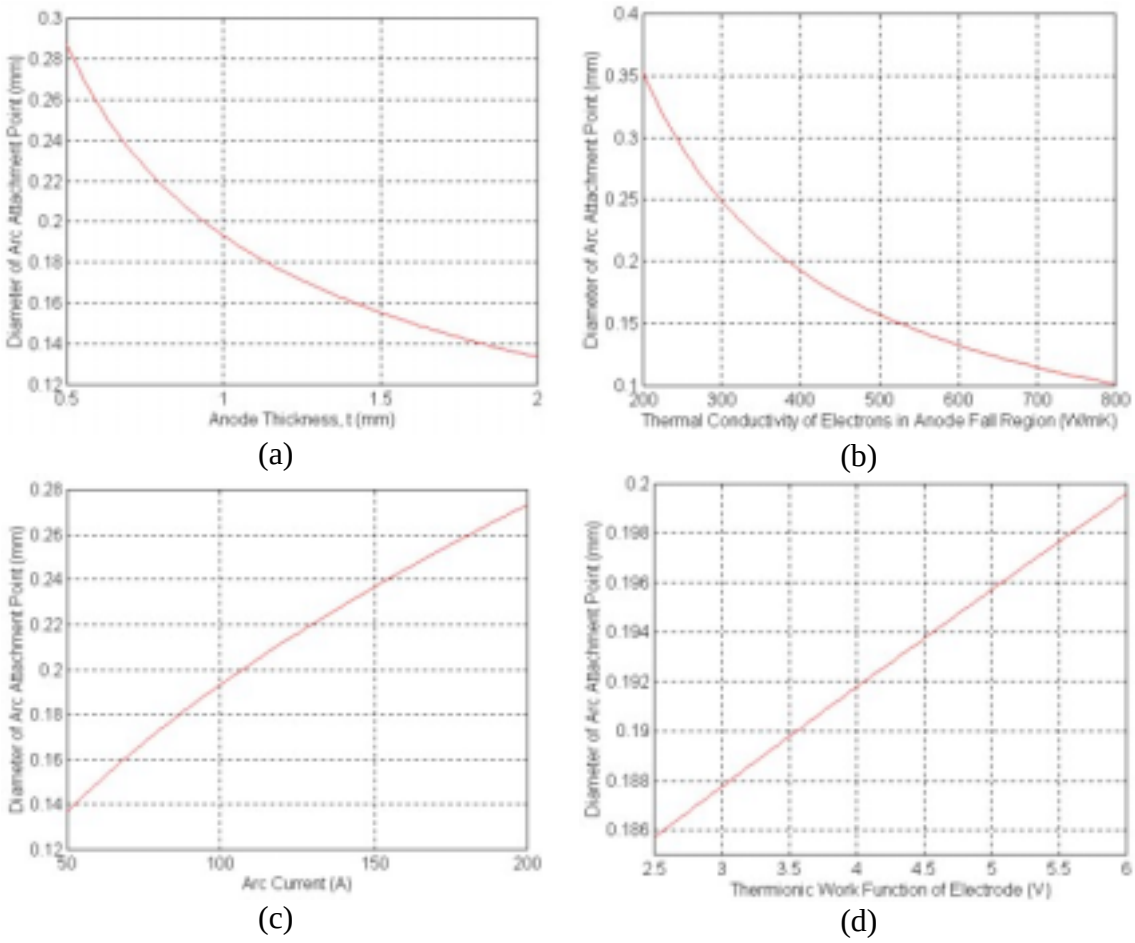


Figure B.12: Diameter of Arc Attachment Point versus Various Parameters

For Figures B.12(c) and (d), an increase in those parameters produces a nearly linear increase in the arc diameter. The trend shown in Figure B.12(c) can be explained in terms of Ohm's law, V=I×R. As current increases, the net effect is that the arc must expand, or reduce its resistivity to maintain a constant voltage. In actuality, both occur. The centerline of the arc reaches a higher temperature, reducing the resistivity of the arc, and the arc expands to accommodate the larger number of electrons passing through (Stouffer, 1989). Figure B.12(c) shows that an increase in the thermionic work function of the electrode causes an increase in the diameter of the arc attachment point. The thermionic work function of a metal is the work in volts necessary to remove a unit

charge of electrons from the surface. This concept can be explained using the Shih equation

$$q_e = j\left[\frac{5kT_e}{2e} + U_a + \phi_a\right], \tag{22}$$

where the thermal energy (first term), kinetic energy gained by electron acceleration through the arc (second term), and the kinetic energy given up by the electrons on impact (third term, where $\phi_a$ is the thermionic work function of the anode), relate to the heat transfer at the point of arc attachment, $q_e$ (Gallimore, 1998). It is important to note that each term is multiplied by the current density j. Since we are only interested in the on-impact effects the equation can be reduced to

$$q_e = j\phi_a . \tag{23}$$

Since an arc will rearrange itself in such a way as to minimize the heat transfer to the anode, increasing the thermionic work function indicates that a reduction in current density will occur (i.e. the arc will expand). This agrees with Figure B.12(d).

## B.5: Conclusions

The aim of this section was to provide an improved understanding of plasma dynamics and the design of plasma generators. Various aspects of plasma were studied, such as chemical, electrical and physical properties. Plasma generation was assumed to be produced by means of an electric arc. For confined arcs, the Elenbaas-Heller equation was used to determine the temperature profile within the constrictor. Also, a model of the arc diameter at the point of anode attachment was studied in relation to various gas and electrode properties for free-burning arcs.

# *Appendix C*

## *Relationships for Momentum Flux Ratio, Mass Flowrate, and Chamber Pressure*

The charts presented in this appendix are meant to serve as an aid for those who are interesting in determining various conditions, such as mass flow rate, not reported in the main body of the dissertation. A Sierra Series 840 mass flow meter was used to collect volumetric flowrate data for methane, nitrogen, ethylene, and air. Accuracy of the mass flowrate measurements is ± 1% for methane and ± 5% for all other gases. The mass flow meter was shipped from Sierra and calibrated to operate with methane and requires a conversion factor when using other gases. The use of this conversion introduces some slight error into the measurements.

Examples of how to use the charts are as follows: Assuming the experiment consisted of the torch operating at 446 kPa (50 psig) exhausting into the atmosphere and the value of the methane mass flow rate is desired. Referring to Figure C.1, a chamber pressure of 446 kPa will allow a mass flowrate of approximately 0.78 g/s to pass through the torch orifice. For tests conducted in the supersonic tunnel, the torch was usually set to run with a momentum flux ratio of 1.17. Referring again to Figure C.1, this corresponds to a chamber pressure of 342 kPa (50 psia). The corresponding mass flowrate can be determined by determining the intersection of 342 kPa line and the mass flowrate trend line. This yields a mass flowrate of 0.58 grams/sec.

The momentum flux ratio is defined as

$$\overline{q} = \frac{\left(\rho u^2\right)_{injec\tan t}}{\left(\rho u^2\right)_{freestream}} = \frac{\left(\gamma P M^2\right)_{injec\tan t}}{\left(\gamma P M^2\right)_{freestream}} \tag{C.1}$$

where P is the static pressure, γ is the ratio of specific heats, and M is the Mach number. The static pressure of the torch can be calculated by

$$P = P_o\left(1 + \frac{\gamma - 1}{2} M^2\right)^{\frac{\gamma}{1-\gamma}} \tag{C.2}$$

where the Mach number at the torch exit is unity and the total pressure is the chamber pressure.

As a final note, the ignition of the torch usually caused a small increase in the torch chamber pressure, generally on the order of 20 kPa when the torch was run at a chamber pressure of 345 kPa (a 5% increase). This was caused by thermal blockage from the arc. The data collected for the charts are from cold flow measurements, but are reasonably close to the actual mass flowrates and momentum flux ratios experienced while the torch was on.

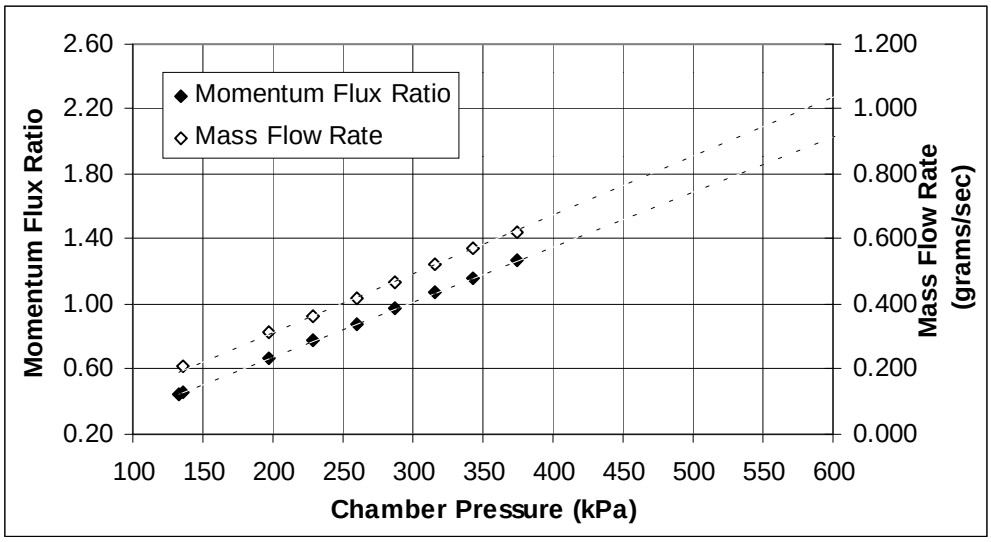


Figure C.1: Conversion Chart for Methane with a 0.178 mm Arc Gap

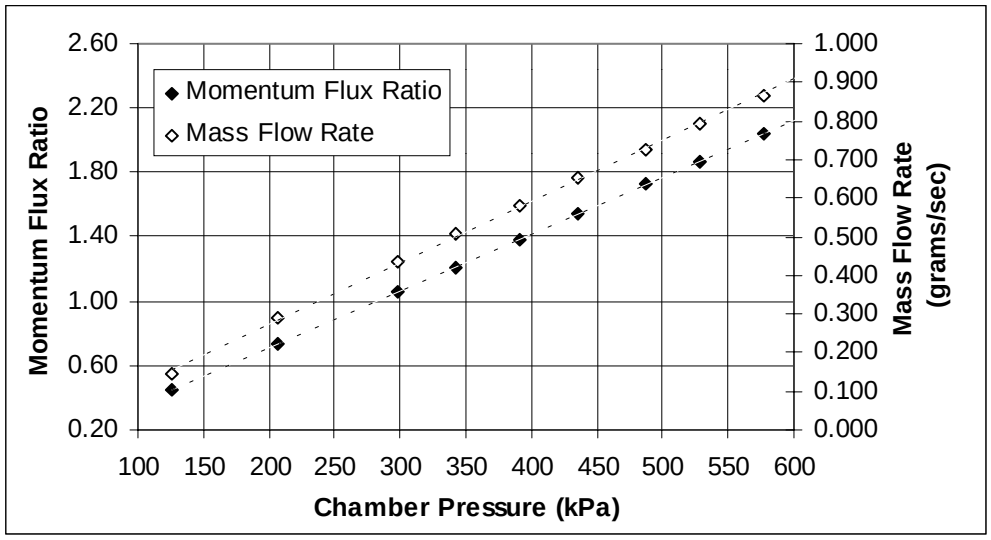


Figure C.2: Conversion Chart for Nitrogen with a 0.178 mm Arc Gap

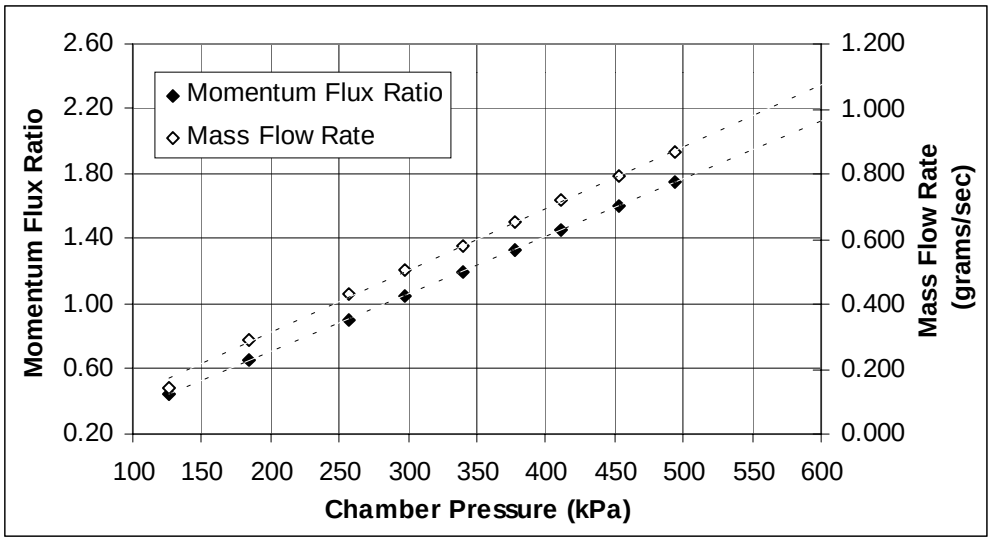


Figure C.3: Conversion Chart for Nitrogen with a 0.267 mm Arc Gap

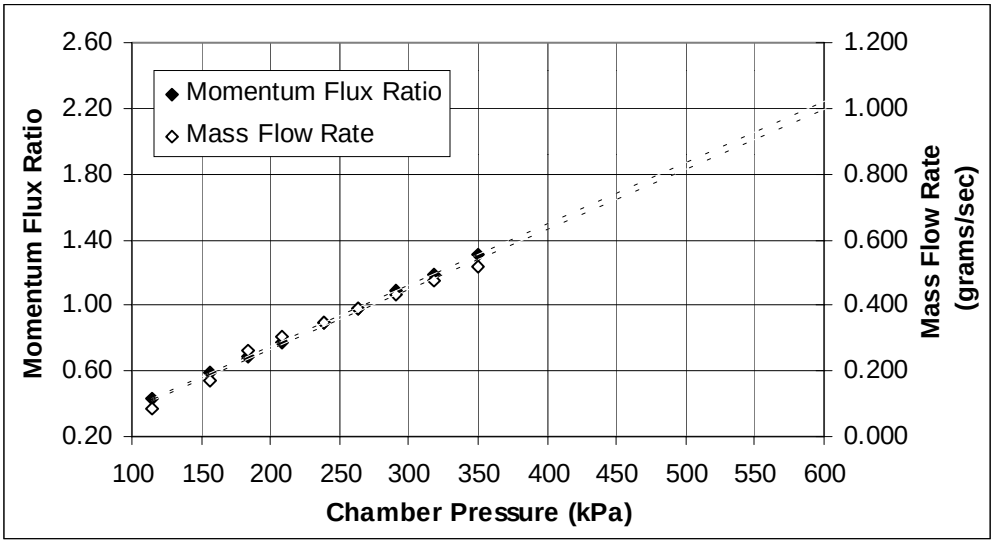


Figure C.4: Conversion Chart for Ethylene with a 0.178 mm Arc Gap

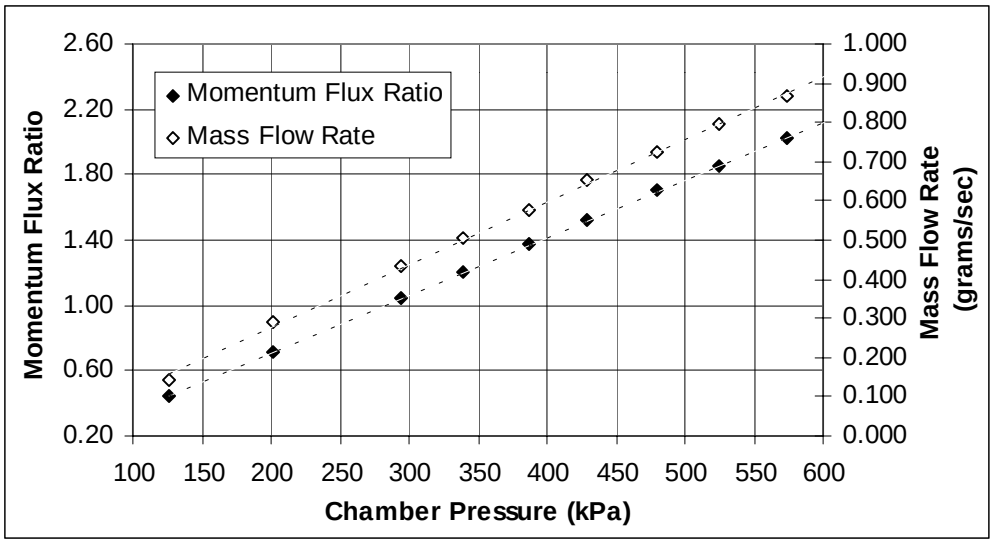


Figure C.5: Conversion Chart for Air with a 0.178 mm Arc Gap

As final note, to nondimensionalize certain data, a parameter $d_{eq}$, or $d_{eff}$ will be used. These stand for the equivalent diameter and effective diameter respectively. For a single circular orifice, the effective diameter is equal to the actual diameter of the torch constrictor (1.59 mm). The effective diameter is related to the equivalent diameter by

$$d_{eff} = d_{eq}\sqrt{C_d}\ , \tag{C.1}$$

where $C_d$ is the discharge coefficient of the torch.

# *Appendix D*

## *Selected Excerpts from*

## *"Numerical Model for Plasma Jet Injection in a Supersonic Crossflow"*

***By Alexandre Perrig***

*Introduction and Editing by Scott Gallimore*

This appendix presents the major results of the work performed by Alexandre Perrig to develop a CFD model that can be used to accurately predict the mixing and penetration characteristics of a methane plasma jet in a Mach 2.4 crossflow. The work presented here incorporates some of the suggested changes made by the present author in Chapter 8 to improve the accuracy of a model developed by Aerosoft, such as implementing a better turbulence model and changing the freestream total temperature to match that of the experimental results. In addition, the study also used a pyramidal approach, that is, the eventual goal of modeling a reacting plasma jet in a supersonic crossflow was reached by making small-steps of increasing complexity and evaluating the results as the process continued. This prevented the problem of obtaining a final solution, which may require changes to the model, and then have the arduous task of determining what the source of the problem actually is. Furthermore, Perrig discusses the assumptions and calculations made by the present author to develop the model. In general, the program demonstrated that a methane plasma jet could be well represented using CFD techniques, but unfortunately only for nonreacting cases. Reacting simulations had poor agreement with experimental results.

### D.1. Methane Injection Model

A model for the methane plasma jet inflow conditions has to be developed. The model pursues two antithetic goals: (1) it has to be as realistic as achievable, and involve as many physical aspects of the injection conditions of the methane plasma, and (2) it has to remain as simple as possible, and be easy to handle for the solver, not to jeopardize the stability of the numerical solution, nor the requested CPU time per iteration. The experimental setup and measurements provide the feedstock conditions, the plasma torch

topology, and some of the plasma physical properties. The following inflow conditions remain to be determined:

(1) Mass-flow of methane at injection port

(2) Injection velocity

(3) Injection pressure

(4) Injection temperature

All these conditions can be deduced from the known experimental data, thermodynamic laws, and a few assumptions. Table D.1 provides methane's feedstock conditions. The mass-flow will be determined first, then the temperature, and finally the remaining inflow thermodynamic conditions.

| $T_{CH4,0}$ | $P_{CH4,0}$ | R | γ |
|---|---|---|---|
| [K] | [kPa] | [$JK^{-1}Kg^{-1}$] | [-] |
| 300 | 344.64 | 519.625 | 1.33 |

*Table D.1: Methane's feedstock conditions*

### D.1.1. Mass-flow

Figure D.1 presents a schematic of the plasma torch in the injection port area, while Table D.2 show the main dimensions of the torch. The topology of the plasma torch, along with the feedstock conditions, provide the information necessary to determine the mass-flow of methane injected into the wind tunnel's test section. The calculations of the cross-flow sections within the plasma torch can be made by referring to Figure D.1.

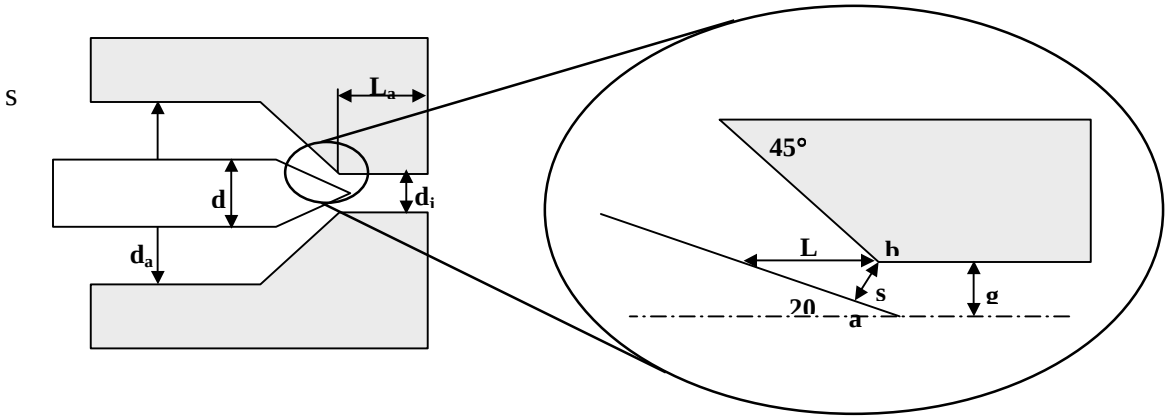


*Figure D.1: Plasma torch main dimensions*

| Anode Internal Ø $d_{ai}$ | Anode Constrictor Length $L_{ac}$ | Anode Constrictor Ø $d_j$ | Cathode Ø $d_c$ | Arc Gap $L_g$ |
|---|---|---|---|---|
| [mm] | [mm] | [mm] | [mm] | [mm] |
| 9.9822 | 2.54 | 1.59 | 3.175 | 0.1778 |

*Table D.2: Main dimensions of the plasma torch*

❑ The anode constrictor area, $A_3$, is given by:

$$A_3 = \frac{\pi}{4} d_j^2 , \tag{D.1-1}$$

and anode interior area, $A_1$, by:

$$A_1 = \frac{\pi}{4}\left(d_{ai}^2 - d_c^2\right) . \tag{D.1-2}$$

The most important section is the smallest cross-flow section between the anode interior surface and the cathode, the gap area $A_2$. The gap region between torch's anode and cathode is magnified in Figure D.1 (right). The slope of the smallest distance between the anode interior angle (point b, on Figure D.1) and cathode's conic tip, s, can be described as a function of the vertical arc gap, g:

$$s(g) = \frac{1}{\sin 20^\circ} g . \tag{D.1-3}$$

Area $A_2$ is the surface of revolution created by the rotation of s (g) - i.e., segment [a, b] - around torch's longitudinal axis, i.e.:

$$A_2 = 2\pi \int_a^b s(g) \sqrt{1 + s'^2(g)}\, dg \tag{D.1-4}$$

Table D.3 summarizes the respective sizes of $A_1$, $A_2$, and $A_3$:

| Anode Interior Cross-Section $A_1$ | Arc Gap Cross-section $A_2$ | Anode Constrictor Cross-Section $A_3$ |
|---|---|---|
| [$m^2$] | [$m^2$] | [$m^2$] |
| $7.034 \cdot 10^{-5}$ | $2.911 \cdot 10^{-7}$ | $1.98557 \cdot 10^{-6}$ |

*Table D.3: Anode cross-section areas*

The area ratio between anode interior cross-section ($A_1$) and arc gap cross-section ($A_2$) is about 241:1. The zone between $A_1$ and $A_2$ acts like a convergent nozzle. Assuming methane to be a thermally perfect gas, the fundamental gas dynamics relations provide the critical pressure ratio, beyond which the flow remains choked throughout the nozzle:

$$\frac{p^*}{p_0} = \left( \frac{2}{\gamma + 1} \right)^{\frac{\gamma}{\gamma - 1}}, \tag{D.1-5}$$

where p* is the critical backpressure, and $p_0$ the feedstock total pressure. For the actual methane feedstock conditions, the ratio is about 0.5. Even though the pressure prevailing beyond section $A_2$ is unknown, there is no doubt that this value will be exceeded. Therefore, the flow is assumed to be choked in section $A_2$.

The mass-flow can then be calculated from:

$$\dot{m} = \rho_{CH_4} A_2 \, a \, , \tag{D.1-6}$$

where $\dot{m}$ is the methane mass-flow, $\rho_{CH4}$, methane's density, and a, the speed of sound at feedstock conditions. With the choked assumption in section $A_2$, Eqn. (D.1-16) may be finally rewritten in the following manner:

$$\dot{m} = \rho_{CH_4,0} \left( \frac{2}{\gamma + 1} \right)^{\frac{\gamma + 1}{2\gamma - 2}} A_2 \left( \gamma R T_{CH_4,0} \right)^{1/2} . \tag{D.1-7}$$

### D.1.2. Jet Bulk Temperature

The following assumptions are made about the plasma jet at its injection port (cross-section $A_3$):

(1) Steady state

(2) Open system

(3) No dissipation

(4) No body forces

(5) Constant velocity, uniform

(6) Methane to be a thermally perfect gas

Considering the jet-centerline (dashed line in Figure D.1), the fundamental equation of Thermodynamic for an open system in steady-state, can be written as [1]:

$$dh + \frac{dc^2}{2} + g\,dz + \delta r = -vdp = \delta e^+ + \delta q^+ + \delta r\,, \tag{D.1-8}$$

where:

- r is the dissipation (from all internal sources),
- g, the gravity constant,
- h, the enthalpy,
- c the jet axial velocity,
- z, the vertical distance roamed by the jet,
- v, the mass-volume,
- $q^+$, the heat-energy received by the gas,
- $e^+$, the work-energy received by the gas.

From assumptions (3)-(5), Eqn. (D.1-8) reduces to:

$$dh = \delta q^+\,. \tag{D.1-9}$$

From assumption (6), it becomes:

$$dh = c_p\,dT = \delta q^+ \tag{D.1-10}$$

Integrating Eqn. (D.1-10), and considering the whole mass-flow of methane, the final result is:

$$\dot{Q}^+_{CH_4} = \dot{m}_{CH_4} c_{pCH_4} \left(T_{bulk} - T_{wall}\right), \tag{D.1-11}$$

where $\dot{Q}^+_{CH_4}$ is the actual heat-power received by the methane from the plasma torch; $T_{bulk}$ is the average temperature of the jet, and $T_{wall}$, the temperature of anode's constrictor walls, assumed to be 400K [2]. $\dot{Q}^+_{CH_4}$ is given by:

$$\dot{Q}^{+}_{CH_4} = \eta_{Torch}\,\dot{Q}^{+}_{el}, \qquad \text{(D.1-12)}$$

where η represents the torch efficiency, $\dot{Q}^{+}_{el}$, the electrical input power to the torch. The torch efficiency is assumed to be 40%: 60% of the electric power is assumed to be lost to the electrodes (Joule effect, Foucault's current, iron losses) or radiation [2]. Finally, combining Eqn. (D.1-11) and Eqn. (D.1-12), the jet bulk temperature may be expressed as:

$$T_{bulk} = \frac{\eta \dot{Q}^{+}_{el}}{\dot{m}_{CH_4} c_{pCH_4}} + T_{wall}\,. \qquad \text{(D.1-13)}$$

Eqn. (D.1-13) has two unknowns: the desired bulk temperature, and the heat transfer coefficient of methane at this temperature. An iterative method has to be used to solve this problem. The flowchart below (Figure D.2) presents the successive steps.

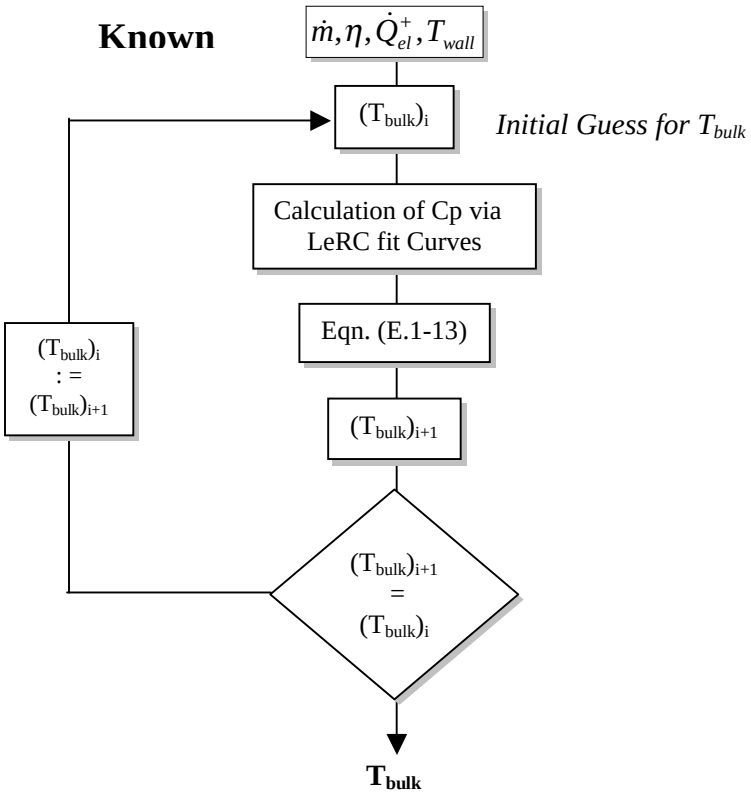


*Figure D.2: Flowchart for the plasma bulk temperature*

An initial guess is chosen for the bulk temperature. The corresponding heat transfer coefficient is determined, according to that temperature, which permits in turn the calculation of a new value for $T_{bulk}$. The new value is used to compute a new value for $c_p$, and so on, until $T_{bulk}$ remains constant. The specific heat of methane is determined at each iteration using the Nasa Lewis Research Center (LeRC) Curve fit, "old" version, valid for a temperature range of 300-5000K [3]. The $a_i$ coefficients are given in Table D.4.

$$\frac{c_{pCH_4}}{\overline{R}} = a_0 + a_1 T + a_2 T^2 + a_3 T^3 + a_4 T^4 . \qquad \text{(D.1-14)}$$

| $a_0$ | $a_1$ | $a_2$ | $a_3$ | $a_4$ |
|---|---|---|---|---|
| [-] | [$K^{-1}$] | [$K^{-2}$] | [$K^{-3}$] | [$K^{-4}$] |
| 3.826 | $-3.979 \cdot 10^{-3}$ | $24.558 \cdot 10^{-6}$ | $-22.733 \cdot 10^{-9}$ | $6.963 \cdot 10^{-12}$ |

*Table D.4: LeRC curve fit coefficients*

### D.1.3. Plasma Temperature Profile

Plasma torch temperature profiles are known to be sharp. The core is extremely hot, while the surroundings are colder - only a fraction of the gas exceeds 3000K.

The spectral emissive power of plasma jets has been measured. The core spectral emissivity is close to that of a black body, well within the range of visible light. The assumption of the black body leads to a core temperature of 6000K [4], a largely accepted value for plasma core. [2,5]. A negative-exponentially-shaped temperature profile can then be assumed. The radial temperature distribution of the plasma at its injection port is chosen to be of the following form:

$$T(r) = Ae^{Br} + C , \qquad \text{(D.1-15)}$$

where r is plasma jet's radius, varying between zero (center) and R (injection port radius); A, B and C are constants to be calculated from three constraints:

(1) The average temperature provided by the calculated temperature profile must be equal to the jet bulk temperature determined in the last part of the present section, i.e.,

$$T_{bulk} = \frac{1}{R}\int_0^R T(r)\,dr\,. \tag{D.1-16}$$

(2) Initial conditions are chosen such as the temperature gradients at the center of the jet, and along anode constrictor's walls, are zero:

$$\left(\frac{dT}{dr}\right)_{r=0} = \left(\frac{dT}{dr}\right)_{r=R} = 0 \tag{D.1-17}$$

(3) Boundary conditions consist from the temperatures of 6000K in the core and 400K along the walls of the anode constrictor:

$$\begin{cases} T(r=0) = 6000\,K \\ T(r=R) = 400\,K \end{cases} \tag{D.1-18}$$

Table D.5 provides the coefficients of Eqn. (D.1-15), obtained for a torch efficiency of 40%, while Figure D.3 shows the resulting temperature profile.

| **R** | **A** | **B** | **C** |
|---|---|---|---|
| [m] | [K] | [$m^{-1}$] | [K] |
| $7.95 \cdot 10^{-4}$ | 5601.3 | $-1.05263 \cdot 10^{4}$ | 398.7 |

*Table D.5: Coefficients for the plasma jet temperature profile*

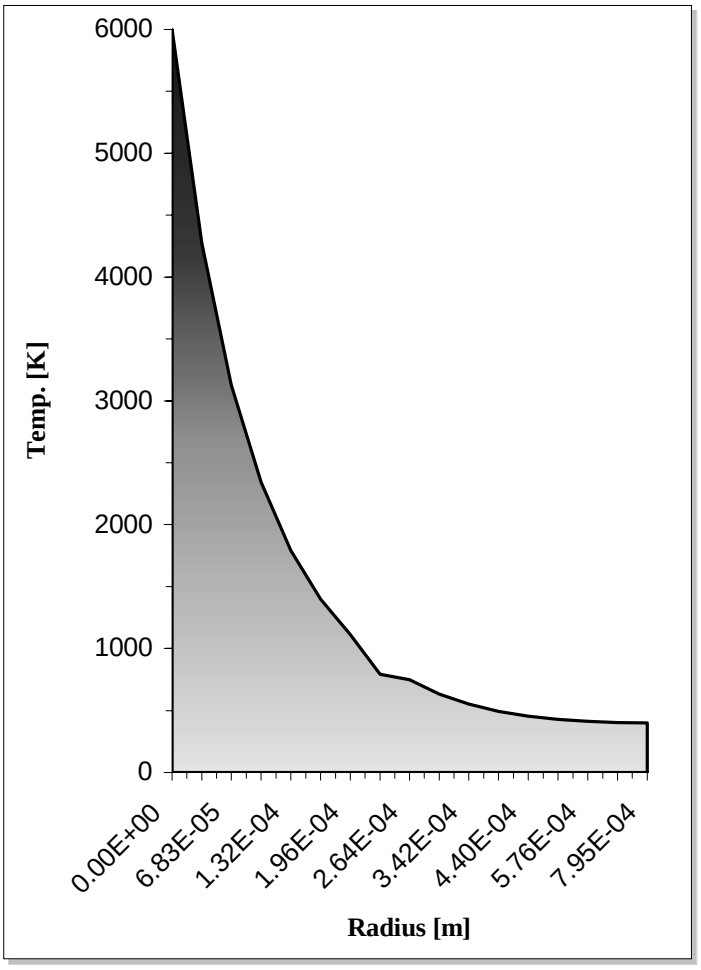


*Figure D.3: Plasma jet core temperature distribution at injection port*

### D.1.4. Methane Jet Exit Conditions

The injection conditions correspond to those presented in section $A_3$ on Figure D.1. Recall that the flow is assumed to be choked in section $A_2$, at feedstock conditions (T= 300K). Throughout the anode constrictor, between section $A_2$ and section $A_3$, heat is being added to the methane flow. The mass flow remains constant - by continuity -, while the gas tends to expand because of the increase in temperature. But, from standard Rayleigh flow consideration [2], at subsonic or supersonic speeds, the amount of heat input cannot be greater than that, for which the leaving Mach number is unity. If the heat addition is too large, the flow will be choked, that is, the initial Mach number will be reduced to a magnitude, which is consistent with the specified amount of heat input [3].

In other words, since the flow is already choked in section $A_2$, it remains choked throughout its travel up within the anode constrictor. The absolute velocity increases, because the temperature, and therefore the volume-flow do, but the Mach number remains unity. The injection conditions are from then on chosen to be choked at bulk conditions, with the same mass-flow as in section $A_2$.

(1) Velocity at injection port

The injection velocity, normal to the injection port, is taken as the sonic speed at bulk temperature, i.e.:

$$v = (\gamma R T_{bulk})^{1/2} \tag{D.1-19}$$

(2) Pressure at injection port

At section $A_3$, the jet is not yet a free jet, that is, the pressure is still higher than the one prevailing in the wind tunnel. Since the jet is choked, Eqn. (D.1-7) is still valid; only the temperature is different.

From Eqn. (D.1-7), the exit static pressure is given by:

$$p_3 = \frac{\dot{m}(R T_{bulk})^{1/2}}{\gamma^{1/2}\left(1+\frac{\gamma-1}{2}M^2\right)^{\frac{\gamma}{\gamma+1}}\left(\frac{2}{\gamma+1}\right)^{\frac{\gamma+1}{2\gamma-2}} A_3} \tag{D.1-20}$$

### D.1.5. Summary and Discussion of the Model

The different parameters searched and determined throughout the present section are presented in Table D.6. The model built for the methane injection intends to match the real injection conditions as reasonably well as achievable. Nevertheless, some points remain open. The most significant concerns are listed below.

| $\dot{m}$ | $T_{bulk}$ | v | $P_3$ |
|---|---|---|---|
| [$Kgs^{-1}$] | [K] | [$ms^{-1}$] | [kPa] |
| $1.715 \cdot 10^{-4}$ | 1084 | 865.53 | 52.24 |

*Table. D.6: Methane jet inflow conditions*

❑ Uniformity of exit velocity

The model does not account for two effects. First, if the flow at the injection port is certainly choked, the bulk temperature assumption to determine the sonic speed at this point is probably too simple [6]. Velocity gradients are likely to occur within the flow due to the very steep temperature profile. Secondly, the viscous effects between the walls of the anode constrictor and the methane flow also modify the velocity profile of the exiting jet. However, including these aspects into the model would considerably complicate the numerical setup and probably produce overwhelming numerical stiffness.

❑ Flow swirler

The real plasma torch is equipped with a device that induces swirling effect within the flow. This helps reduce the likelihood of hot spots on the electrodes, thus prolonging their life. The assumption of constant and uniform velocity is rough, but allows modeling half of the test section, hence significantly reducing the computational cost.

❑ Temperature profile

The exact profile is not known. The profile assumed is intended to match as well as possible the real temperature profile. Even if this assumed profile is not perfect, it represents the best choice available.

❑ Dissociation throughout the anode constrictor

The greatest amount of heat transfer between the electrodes and the flow occurs in an area that corresponds roughly to the section $A_2$ on Figure D.1. That means that the methane flow already experiences dissociation and chemical reactions throughout its travel in the anode constrictor. The plasma (dissociated molecules, radicals) appears earlier in the real torch than it does in the model, where pure methane is injected.

### D.1.6. Injection Model for GASP

The injection port in GASP is modeled as a special inflow boundary condition. The inflow conditions are imposed for each grid point by means of the conservative

primitive vector **q**. Since the temperature is not a conservative primitive, the only way of imposing the calculated temperature profile consists in imposing the point-wise density corresponding to the node radial position. The density is evaluated for each point using the law of thermally perfect gases, with a gas constant independent of temperature. The accuracy is sufficient considering the assumptions made to build the plasma injection model.

## D.2. Chemical Model for the Plasma Jet

This section provides a short description of the chemical model chosen for the plasma jet. A brief review of the basics of chemical kinetics of combustion processes is also provided.

### D.2.1. Chemical Background: Chemical Kinetics

Although a combustion process may include many physical processes, it is essentially and ultimately a chemical reaction. The chemical reaction speed is affected by the temperature, pressure, composition of the reacting mixture, and by the presence or the absence of surfaces.

#### D.2.1.1. Reaction rate

One of the most basic concepts concerning chemical reaction rates is the law of mass action, which relates the rate of a reaction –or the time of change of the reactant species concentration- to the concentration of the reactant species. This can be illustrated with the generic reaction

$$aA + bB \leftrightarrows cC + dD, \qquad \text{(D.2-1)}$$

in which a moles of molecule A combine with b moles of molecules B to form c and d moles of products C and D. The stoichiometric coefficients of the atomic balance equation (a, b, c, and d) are also called the reaction molecularity. The law of mass action states that, for a homogeneous system, the rate of chemical reaction is proportional to the product of the concentration of the reactant species raised to their respective

stoichiometric coefficients. For Eqn. (D.2-1) above, the rate of the forward reaction would be

$$r_f = k_f [A]^a [B]^b \tag{D.2-2}$$

Reciprocally, by the law of mass action, if the reaction is reversible, the rate of the reverse reaction is

$$r_r = k_r [C]^c [D]^d \tag{D.2-3}$$

Thus, $k_f$ is the rate constant, or specific reaction-rate coefficient, or simply rate coefficient for the forward reaction, and $k_r$ is the specific reaction-rate coefficient for the reverse reaction. The molar concentrations [A], [B], [C], and [D] may be expressed in several ways –Moles of i species/Total Volume, Moles of i species/Total Moles, Partial Pressure.

*D.2.1.2. Order of Reaction*

An 'elementary reaction' is characterized by its order of reaction. Reactions of the first order involve changes of a single molecule into products. Reactions of the second order, or bimolecular reaction, involve the reaction between two molecules, or between an atom – or a radical - and a molecule, to yield the products. Third order reactions involve interactions between three species simultaneously. The order of reaction is a means of classification of the various types of rate laws.

❑ Zero order

$$-\frac{d[x]}{dt} = k_k . \tag{D.2-4}$$

❑ First Order

$$-\frac{d[X]}{dt} = k_f \left([A]_0 - [X]\right). \tag{D.2-5}$$

❑ Second Order

$$-\frac{d[X]}{dt} = k_f \left([A]_0 - [X]\right)^2$$
$$-\frac{d[X]}{dt} = k_f \left([A]_0 - [X]\right)\left([B]_0 - [X]\right) \quad . \qquad \text{(D.2-6)}$$

❑ Third Order

$$-\frac{d[X]}{dt} = \left([A]_0 - [X]\right)^3, \qquad \text{(D.2-7)}$$

where $[A]_0$ and $[B]_0$ represent the initial concentrations of the reactants.

*D.2.1.3. Temperature Dependence of Reaction Time*

For many reactions of importance to combustion systems, $k_f$ is a strong function of temperature. If the concentrations in the reaction system are kept constant, but the temperature of the system is increased, there is usually a marked increase in the rate coefficient and thus the reaction rate. According to Arrhenius, the temperature dependence is expressed as

$$k_f = ZT^b e^{(-E_a/RT)}, \qquad \text{(D.2-8)}$$

where $E_a$ is Arrhenius activation energy, which can be thought of as the energy barrier that must be overcome if a successful collision of two molecules A and B is to lead to final products C and D. The lower the activation energy, the easier a reaction is accomplished. Ea/RT is also known as the Zeldovitch number. Z is a constant depending on the number reactant moles [$m^3$/Kg·mol/s/$K^n$]. These basic concepts are used to form reaction mechanisms to model chemical reactions. The chemical kinetics forms the elementary steps needed in simple to complex representations.

### D.2.2. Oxidation Model for Methane

*D.2.2.1. Investigation of NO Formation*

Several studies were carried out in the ’70’s about pollution formation in jet engine combustors. The nitric Oxide (NO) formation mechanism was studied intensively, because it was -and still is - one of the limiting factors for increasing the combustion temperature, and thus the thermal efficiency of gas turbines. The only chemical model available at the time was Zeldovitch’s model, which stemmed from the late ‘30’s. This 2-step model for NO formation proved incomplete, brought to light by improvement of the measurement techniques [7]. The importance of many of the intermediate atoms and free radicals that are an inherent part of any combustion process must be taken into account. During fuel-rich hydrocarbon combustion, hydrocarbon fragments, radicals, and a variety of oxygenated species are produced. Accounting for them is a potential importance in adequately representing the fuel oxidation process.

Bowman and Seery (1972) [7], experimentally investigated the shock-induced combustion of a mixture of methane, oxygen, and nitrogen at temperature range of 2100-2500K, in order to determine the mechanism for NO formation during combustion of hydrocarbon fuel. The preliminary step of their study consisted of developing a model for the methane-oxygen reaction. Spectroscopic techniques were used to measure time-histories of concentrations of species. Time-rates change of species concentrations and thermodynamics properties during the reaction were calculated by numerically integrating the coupled reaction kinetic, state and energy equations. Their 14-step model appeared to adequately predict the methane-oxygen chemistry for the conditions of the experiments.

#### D.2.2.2. Methane Combustion

Usually, the behavior of hydrocarbons in homologous series is very similar, especially regarding the ignition delay time (IDT). Methane ($CH_4$), the simplest hydrocarbon, is the first hydrocarbon of the *alkane* series. To the contrary of other hydrocarbons, its ignition delay time is significantly longer than that of the higher hydrocarbons in the same series. This phenomenon is due to two peculiarities of the $CH_4$ molecule:

(1) Absence of C-C connections

The methane molecular structure is

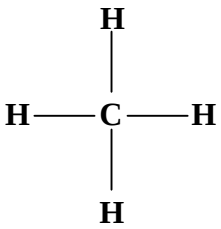

, whereas higher *alkanes* are.

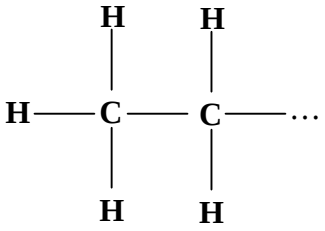

The C-H connection requires significantly more energy to be broken than the C-C connection.

(2) Presence of the methyl radical ($CH_3$) among methane's decomposition products. This radical is associated with the termination step of the combustion chain reaction.

Edelman and Harsha (1978) [8] modified the Bowman-Seery model to integrate the NO formation mechanism. The new model is a 13-species and 11-step reaction.

Experiments confirmed the adequacy and accuracy of Bowman-Seery/Eldman-Harsha methane combustion model, in spite of the existence of a controversy over the importance of some species and reactions governing fuel oxidation process. The model does not account for the formation and chemistry of formaldehyde (HCHO), hydroxyl radical ($HO_2$), hydrogen peroxide ($H_2O_2$), or other intermediates as cyanide (CN). Table D.7 presents the different reactions of the model, with Arrhenius relation's coefficients. The key-aspects of this chemical model are

(1) Crucial basic $H_2$-air reactions

(2) CO oxidation is controlled by the hydroxyl radical (OH)

(3) Methyl radical dominates the initial phase of the oxidation process.

| Reaction | Z | b | $E_a/R$ |
|---|---|---|---|
| 1. $CH_4 + M \leftrightarrows CH_3 + H + M$ | $2 \cdot 10^{17}$ | 0 | $44.5 \cdot 10^3$ |
| 2. $CH_4 + OH \leftrightarrows CH_3 + H_2O$ | $2.8 \cdot 10^{13}$ | 0 | $2.5 \cdot 10^3$ |
| 3. $CH_4 + O \leftrightarrows CH_3 + OH$ | $2 \cdot 10^{13}$ | 0 | $4.64 \cdot 10^3$ |
| 4. $CH_4 + H \leftrightarrows CH_3 + H_2$ | $6.9 \cdot 10^{13}$ | 0 | $5.95 \cdot 10^3$ |
| 5. $CH_3 + O_2 \leftrightarrows H_2O + CHO$ | $2 \cdot 10^{10}$ | 0 | 0 |
| 6. $CH_3 + O \leftrightarrows CHO + H_2$ | $1 \cdot 10^{14}$ | 0 | 0 |
| 7. $CHO + OH \leftrightarrows CO + H_2O$ | $1 \cdot 10^{14}$ | 0 | 0 |
| 8. $CHO + M \leftrightarrows H + CO + M$ | $2 \cdot 10^{12}$ | 0.5 | $14.4 \cdot 10^3$ |
| 9. $O + N_2 \leftrightarrows NO + N$ | $1.4 \cdot 10^{14}$ | 0 | $3.79 \cdot 10^{4(1)}$ |
| 10. $N + O_2 \leftrightarrows NO + O$ | $6.4 \cdot 10^9$ | 1 | $3.14 \cdot 10^3$ |
| 11. $N + OH \leftrightarrows NO + H$ | $4 \cdot 10^{13}$ | 0 | 0 |

Table. D.7: Bowman-Seery/Edelman-Harsha Model for methane combustion in air. M is a molecule.

*D.2.3. Plasma Jet and Combustion Model*

A plasma jet is composed of a blend of radicals, broken molecules, ions, and ionized molecules. Basically, when this hot plasma encounters the air-stream, a combustion process is initiated. These two aspects –blend of radicals stemmed from methane and combustion in air- are present in the Bowman-Seery/Edelman-Harsha chemistry model, making it very suitable for the plasma jet. The relative simplicity of this model is also attractive from the CFD point of view – computational cost! The methane oxidation model is coded in GASP using the ad hoc tool.

*D.3. Non-Reactive Injection Cases*

D.3.1. Principle

The simulation of a hot, but non-reactive methane injection is investigated for both turbulence models. The same temperature profile and inflow conditions as the plasma jet modeled in the previous section are used. This permits a quick glance at the behavior of each model, providing a good sample of what is to be expected from the reactive-flow simulation. Above all, it is much cheaper in computational cost than modeling the reactive-flow.

(1) Note that Zeldovitch's constant, $E_a/R$, is $3.79 \cdot 10^4$ in accordance to Bowman-Seery, and not $E.79 \cdot 10^3$ as in Edelman-Harsha.

### D.3.2. Numerical Setup

*D.3.2.1. K-ε Model*

Figure D.4 provides an isometric view of the computational domain, and its main dimensions. The injection port is located 25% of the domain's length downstream of the inflow boundary, providing enough room for the compressible effects that are likely to occur ahead of the jet. The flow is assumed to be symmetric, with the axis of symmetry passing through the middle of the plasma torch's anode constrictor – the injection port.

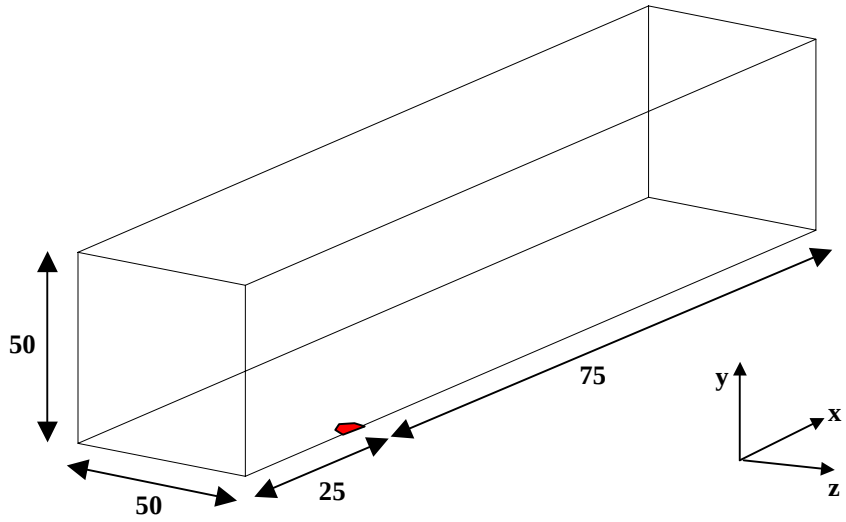


*Figure D.4: CFD domain for the plasma jet injection, K-ε case (dimensions are in [mm])*

The spatial discretization features a 4-block elliptic PDE hybrid C-H structured mesh. The number of grid points is kept as limited as possible. Only the regions of physical interest are refined. An isometric view of the domain and the boundary condition chosen are provided by Figure D.5.

The injection region is modeled as conic-shaped C-H grid. The conic shape is intended to conserve a reasonable cell aspect ratio at the domain's top, where the grid density is low. The total number of cells is less than 100,000 and the aspect ratio of the cells never exceeds two orders of magnitude. The vertical node distribution is identical to that of the flat plate used to calculate the velocity profile to be imposed as inflow boundary. This guarantees the value of $y_1^+$ to be correct and the velocity profile to perfectly match the grid. The numerical approach is summarized in Table D.8.

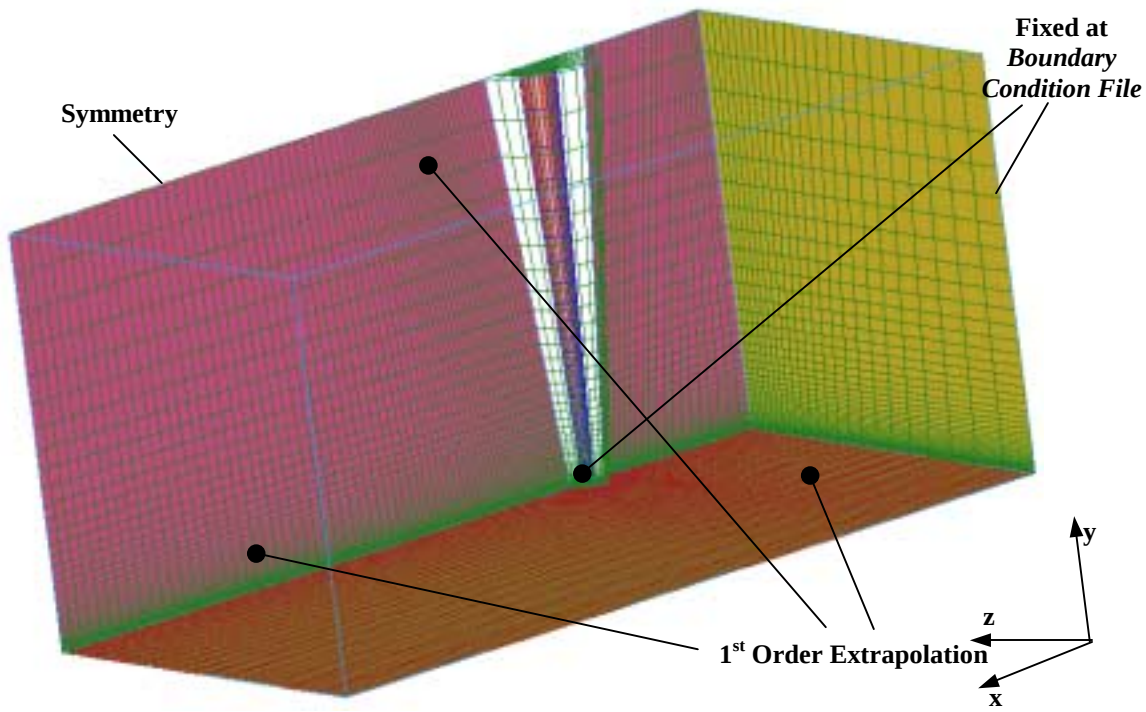


FigureD.5: Isometric view of the mesh, non-reactive K-ε case

| Governing Equations | Flux Function | Spatial Reconstruction | Limiter | Time-Integration | Sweeping Strategy |
|---|---|---|---|---|---|
| RANS (Thin-Layer) | Rho | 3rd order Upwind Biased | Min-Mod | Jacobi, Inner Iterations | Backward K, 3-level Sequencing, Parallel Processing |

Table D.8: Numerical setup for the non-reactive methane injection, K-ε turbulence model

The numerical model makes extensive use of the different convergence-enhancement features offered by GASP:

(1) Parallel processing. The main block of the mesh is decomposed in three sub-zones of equal size to improve the CPU-efficiency of the 6 processors used.

(2) 3-level mesh sequencing.

(3) The grid is swept from the region of weakest gradients to the region of strongest gradients in order to improve the numerical stability.

(4) The simulation is initiated with strong limiters on the turbulence parameters to avoid any sudden divergence at an early stage of the resolution.

### *D.3.2.2. K-ω Model*

The computational domain chosen for this turbulent model exhibits the same structure as the K-ε model. The overall dimensions are reduced, the height by 40% (30mm) and the width by 20% (20mm). The spatial discretization is also similar with the k-ε case. The isometric view of the elliptic PDE hybrid C-H mesh (Figure D.7) gives an appreciation of the significant grid density in the near-wall region and the *hyperbolic tangent* nodes distribution in the vertical direction. The total cell number is about 123,000, i.e. 25% more than the k-ε case. The boundary conditions are the same as for the K-ε case.

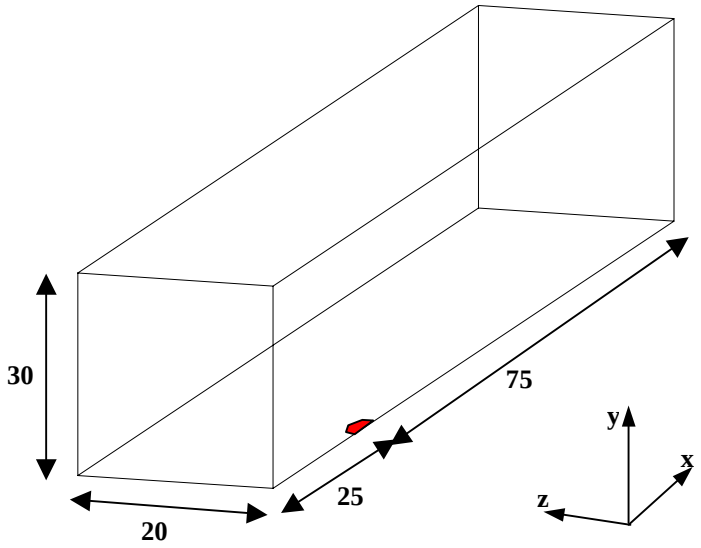


*Figure D.6: Computational domain for the plasma jet injection, k-ω case*

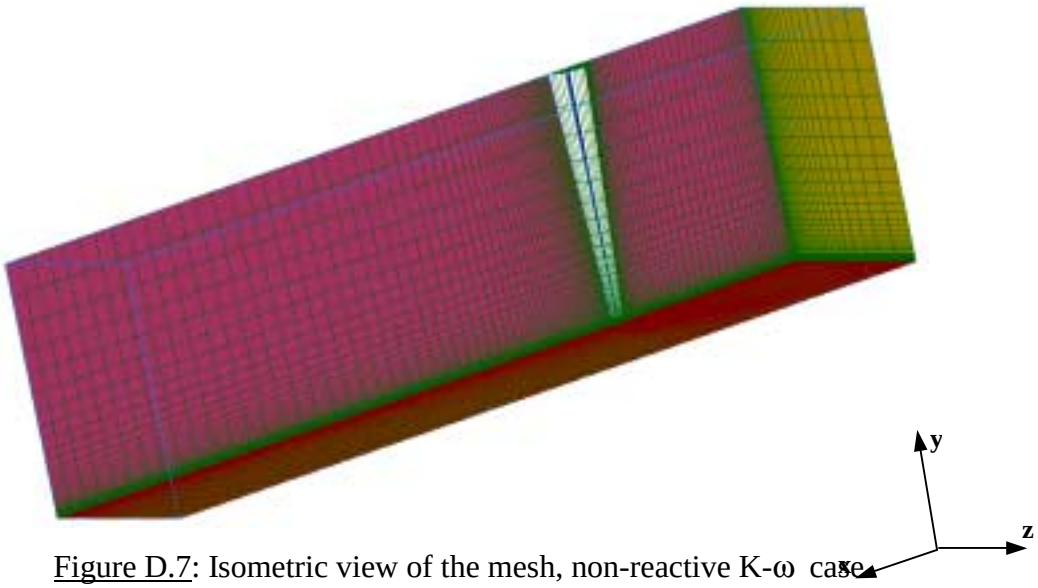


Figure D.7: Isometric view of the mesh, non-reactive K-ω case

The node repartition in the cross-flow section is identical to that of the 3-D nozzle used to determine the velocity profile to be imposed at the inflow boundary – one-to-one matching of the primitive vector **q** and respect for the value of $y_1^+$. A H-grid is used to discretize the core of the plasma jet (opposite, Figure D.8), increasing the grid resolution where the jet temperature profile is the sharpest. The numerical setup is summarized in Table D.9 below

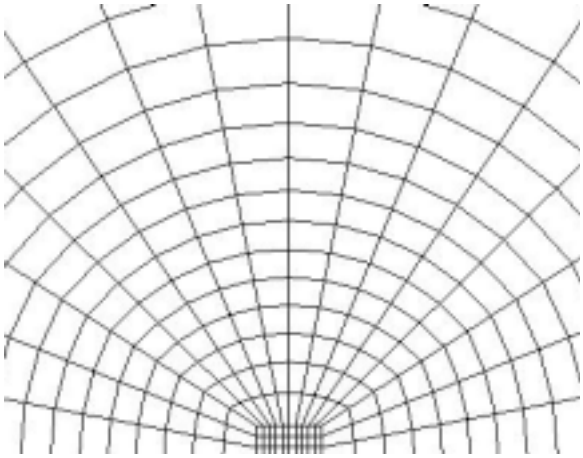

*Figure D.8: Detail of the mesh, injection port*

| Governing Equations | Flux Function | Spatial Reconstruction | Limiter | Time Integration | Sweeping Strategy |
|---|---|---|---|---|---|
| RANS (Thin-Layer) | Roe | 3rd Order Upwind Biased | Min-Mod | 2 F-AF | Backward K Forward K, Parallel Processing |

Table. D.9: Numerical setup for the non-reactive methane injection, K-ω case

The numerical approach presents some marked differences in comparison with the K-ε case. The different convergence optimization strategies used are listed below.

❑ Parallel processing. The main zone of the mesh is decomposed in two sub-zones to improve the efficiency of the parallel processing.

❑ No mesh sequencing is used. This guarantees the value of $y_1^+$ to remain correct throughout the resolution of the problem. It also appears that mesh sequencing does not improve the numerical behavior of the K-ω turbulence model (see next section).

❑ Sweeping strategy. A double-sweep approach is used, i.e. the entire grid is swept twice at each iteration, once from the weakest gradients region to the strongest gradients region – backward - and then in the reverse direction – forward -. The CPU cost is significantly increased, but the stability of the numerical solution is dramatically improved, and the total number of iterations required to converge the solution is reduces.

❑ The problem is initiated with strong limitations on the turbulence model. The maximum allowed eddy viscosity/laminar viscosity ratio is limited to very small values at the beginning of the problem, and progressively increased (again, discussed further in the next section).

**D.3.3. Results and Discussion**

The results obtained for the non-reactive flow provide a good means of comparing the two turbulence models. Some comparisons with the experimental data can also be performed. The results are to be compared on account to: (1) the convergence history and the numerical behavior, (2) the resolution of the shock system engendered by the encounter between the methane jet and the air-stream, (3) the initial penetration of the jet near the injection port, (4) the penetration and the total temperature mapping at the exit boundary of the CFD domain, and (5) the turbulence kinetic energy and mixing mapping of the jet near the injection port.

*D.3.3.1. Convergence History*

The two turbulence models are compared based on their respective numerical behavior. This serves only to examine the hardware efficiency of each approach - the ease at which each reaches a solution. It is not about the physical exactness of the solutions obtained.

❑ K-ε Turbulence Model

Figure D.9 shows the evolution of the $L_2$ norm residuals normalized throughout the calculation. The three different blocks used are clearly seeable.

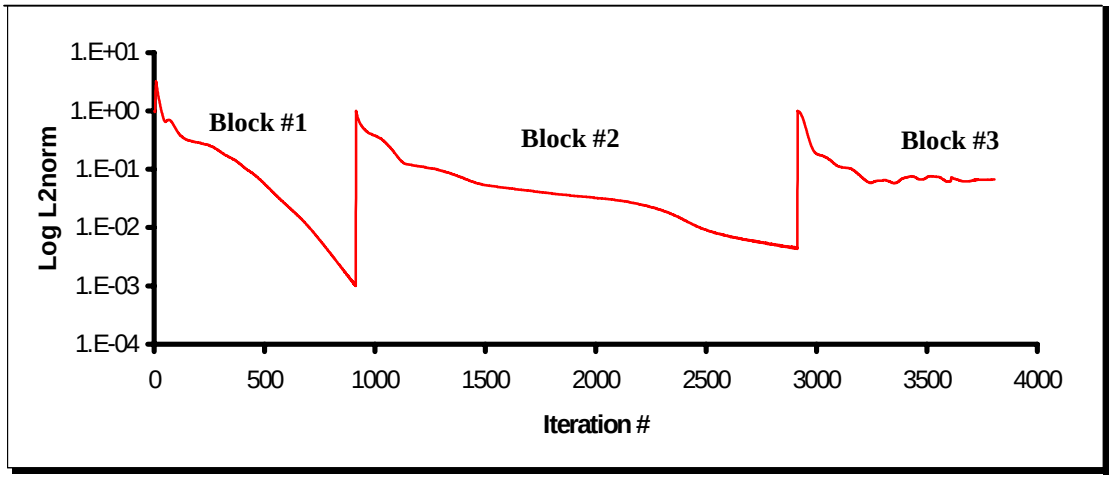


*Figure D.9: Convergence history, non-reactive flow, K-ε turbulence model*

The coarser grid – block #1 - allows fair convergence speeds, reaching a three orders of magnitude decrease in less than 1,000 iterations.

The convergence on the medium grid level – block #2 - is more problematic. A severe restriction must be applied on the CFL criterion – down to $10^{-3}$ - to avoid a tendency of swift divergence. About 2,000 iterations are needed to reach two orders of convergence.

On the finer grid – block #3 -, the initial residual behavior is encouraging, but, as the $L_2$ norm reaches about 1.5 orders of convergence, the whole numerical solution becomes unstable. Even with an extremely restrictive CFL criterion, the problem is impossible to overcome. A deeper investigation reveals the responsible zone to be the near-injector region. This could evidence a problem due to the use of the *wall function*, which cannot solve the highly 3D effects caused by the encounter between the air-stream and the methane jet. The solution is nevertheless considered 'converged' since the rest of the grid reaches a fair convergence. The simulation is performed on six processors of a Silicon Graphics *Origin 2000* computer, with a parallel efficiency of 70%.

### ❑ K-ω turbulence Model

Figure D.10 shows the evolution of the $L_2$ norm for the K-ω turbulence model. The start of the simulation is extremely stiff, the system presenting a tendency to diverge bluntly after about ten iterations. The only way to overcome this obstacle is to initiate the

calculation imposing a strong limitation of the eddy viscosity/laminar viscosity ratio - the flow behaves therefore as a highly viscous flow - and to adopt a double-sweep strategy. Mesh-sequencing must be avoided as well. After one order of convergence, the viscosity ratio limitation is partially removed and, after 750 iterations, completely suppressed. This permits a smooth, well-behaved transition to 3 orders of convergence. The double-sweep resolution is expensive in CPU time and requires large quantities of memory, but appears to be extremely robust and effective regarding the number of iterations necessary to converge the solution. The case is run on four processors on SGI *Origin 2000*, with a parallel efficiency of 98%.

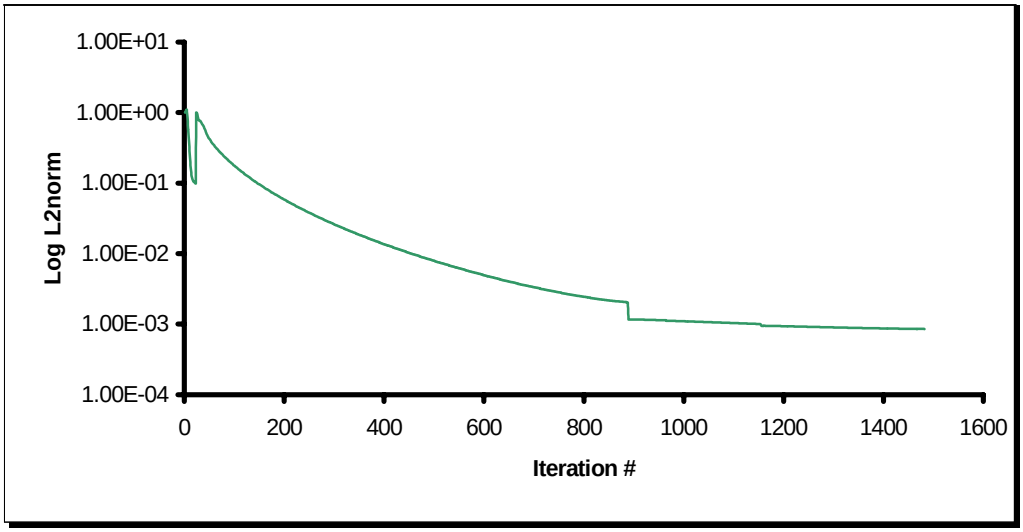


*Figure D.10: Convergence history, non-reactive flow, K-ω turbulence model*

As expected, the K-ε turbulence model presents more numerical stiffness than the K-ω model. The final convergence magnitude is poor in comparison with the K-ω model. The simulation requires constant monitoring of the residuals and frequent intervention on the CFL criterion to preserve the monotonicity of the solution. The question remains open about the responsibility of the *wall functions* in such a highly 3D flow configuration. The K-ω is much easier to converge once the initial stiffness is overcome. The solution is robust throughout the resolution of the problem.

*D.3.3.2. Jet Exit*

The focus here is on the methane jet near the injection port. The contour plots of the total temperature (Figure D.11 (a) and (b)) provide some interesting tendencies of each turbulence model. The two cases are compared based on: (1) the initial path, and (2) the initial penetration and the evolution of the total temperature in the plume.

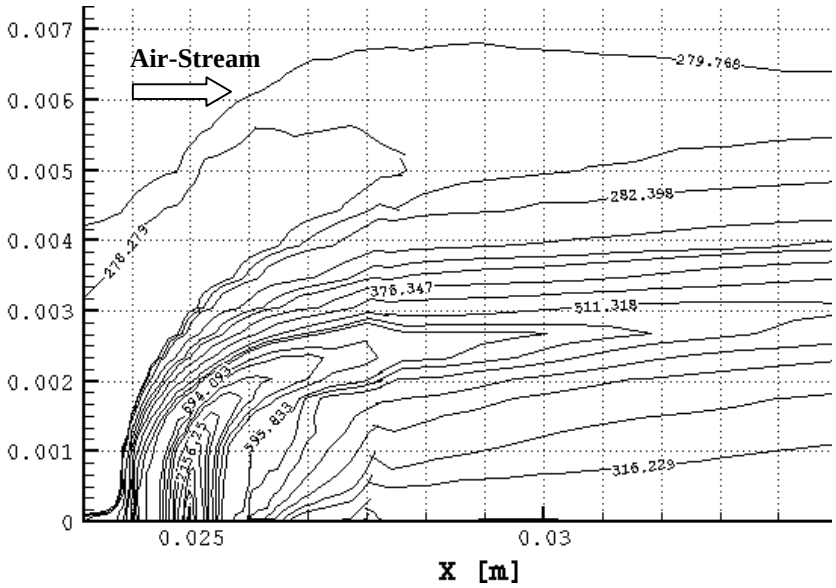


*(a) K-ε turbulence model*

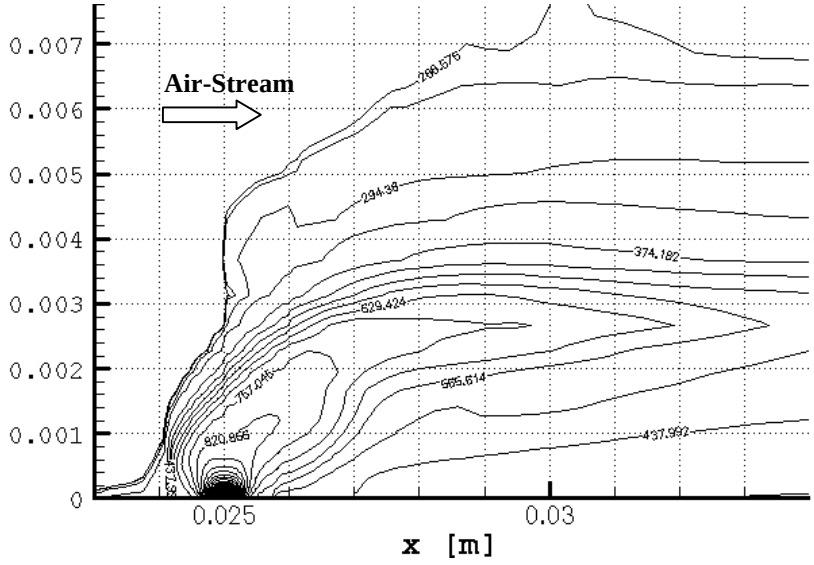


*(b) K-ω turbulence model*

<u>Figure D.11:</u> *Total temperature field near the injection port*

(1) Initial path

The jet plume exhibits a very similar shape for both cases. The trajectory of the methane particles is vertical up to 1mm off the injection port before to starting to mix with the dominant throughflow. The path predicted by the K-ω model looks slightly flatter than the path predicted by the K-ε model, but the difference is not significant.

(2) Initial penetration

The differences are more noticeable. The K-ε case presents a much higher penetration –the methane jet is candle-shaped. The jet plume predicted by the K-ω model seems not to be able to burst the lower portions of the boundary layer. About 1mm above the injection port, the total temperature is still more than 2,000K for the K-ε case, whereas it is already 800K for the k-ω case. Further downstream, the K-ε turbulence model predicts a faster cooling of the jet than the K-ω model, for which the total temperature drops slower (see Figure D.11, for example, at x = 0.028m).

*D.3.3.3. Shock System*

Figure D.12 (a) and (b) show the CFD results for the mixture density variation within the test section. The jet plumes are easily identified, while the oblique shocks are directly upstream (the red/orange areas). Both turbulence models predict very similar shock structures.

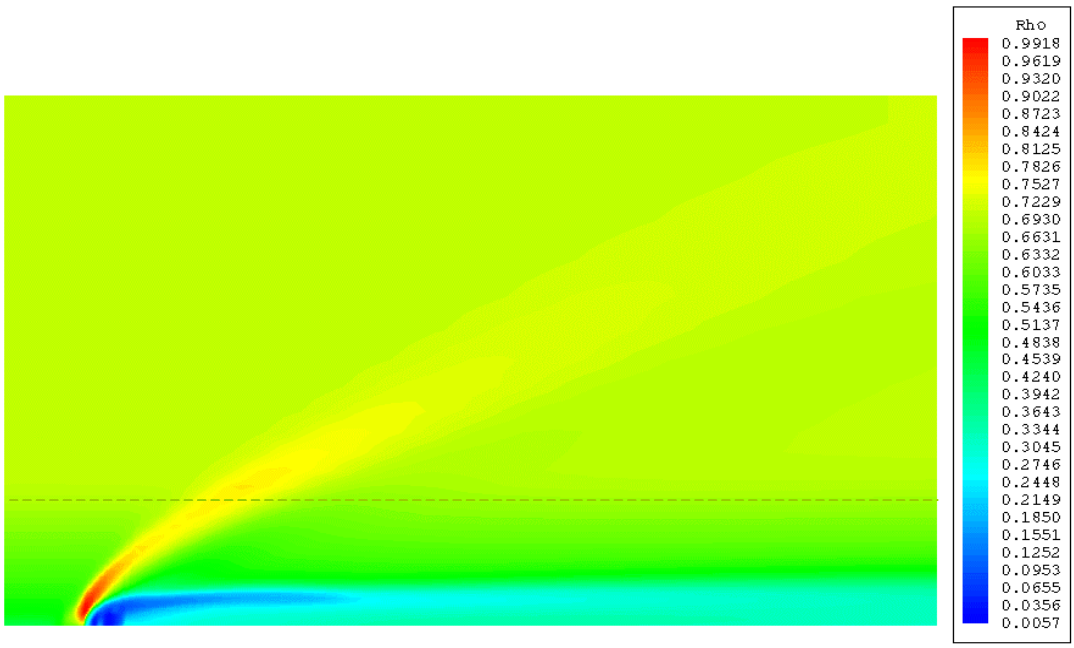


*(a) Shock system, K-ε turbulence model*

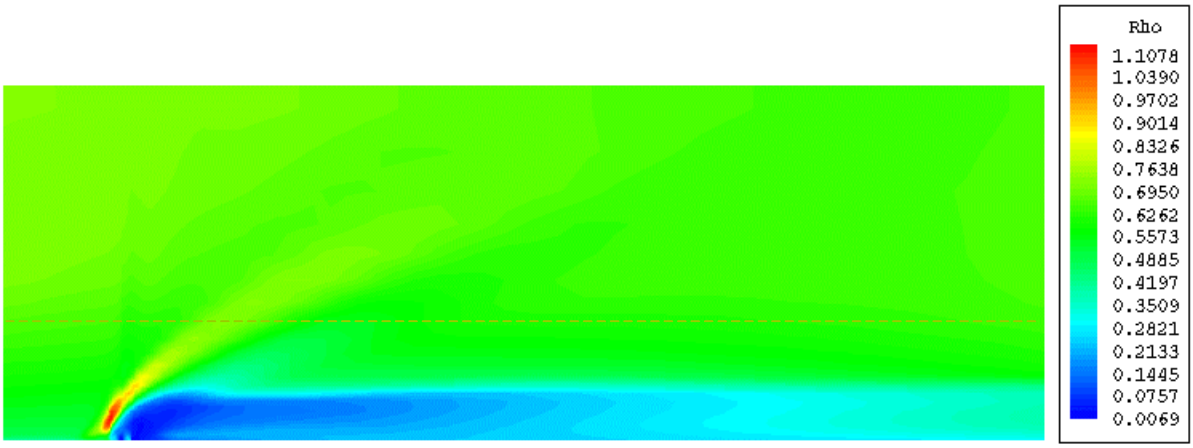


**(b) Shock system, K-ω turbulence model**

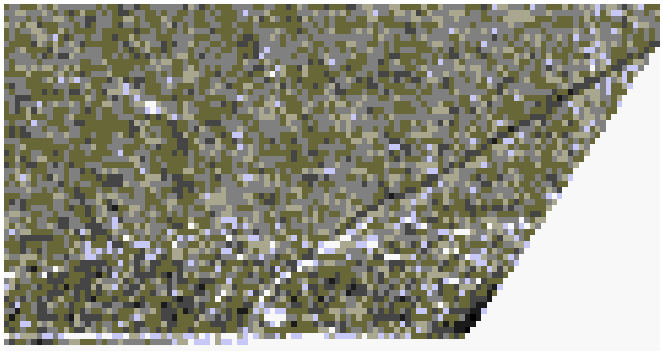

*(c) Shadowgraph showing the shock angle, real test section*

*Figure D.12: Shock systems*

The oblique shock angle – measured from the edge of the boundary layer, identified by the dashed lines - is 31° in both cases, matching the experimental data very well. Figure D.12 (c) is a shadowgraph of the actual shock structure, which although grainy, is easily identified. The shocks are detached and located at the same distance ahead of the injection port - visible as a low-density dot. The subsonic portion of the boundary layer is clearly visible at the root of the shocks. The K-ω turbulence model predicts a slightly higher value for the thickness of the subsonic portion of the boundary layer than the k-ε model. This is another expression of the effects of the use of *wall functions* as boundary conditions.

Among the differences, the most significant is the evolution of the methane density throughout its path in the test section. The K-ε model predicts a rapid increase of the density, confirming the rapid cooling of the jet observed near the injection port, while for the K-ω model, the density remains very low. A strong interaction with the floor is also visible for this case.

*D.3.3.4. Penetration*

Figure D.13 (a) and (b) compares the mapping of the total temperature at the same location - 49.8 injector diameters downstream of the injection port - obtained numerically (left) and experimentally (right). Even though the CFD results do not take into account any chemical reaction, some conclusions can be drawn about the ability of the turbulence model to adequately capture the physics of the flow.

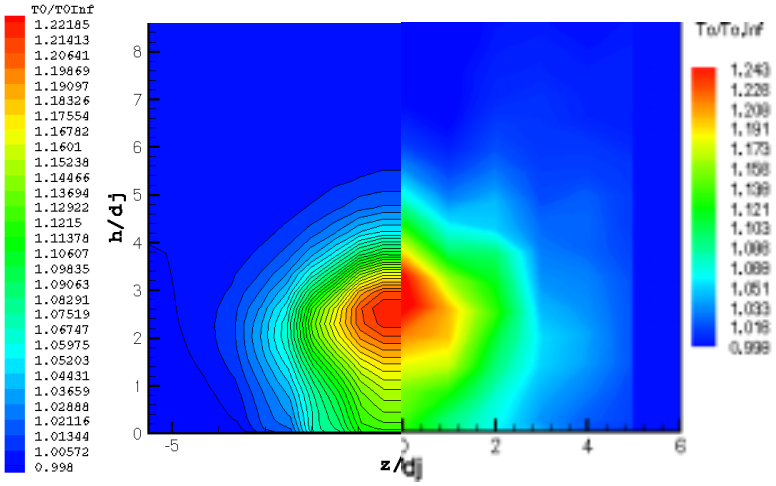


*(a) K-ε turbulence model*

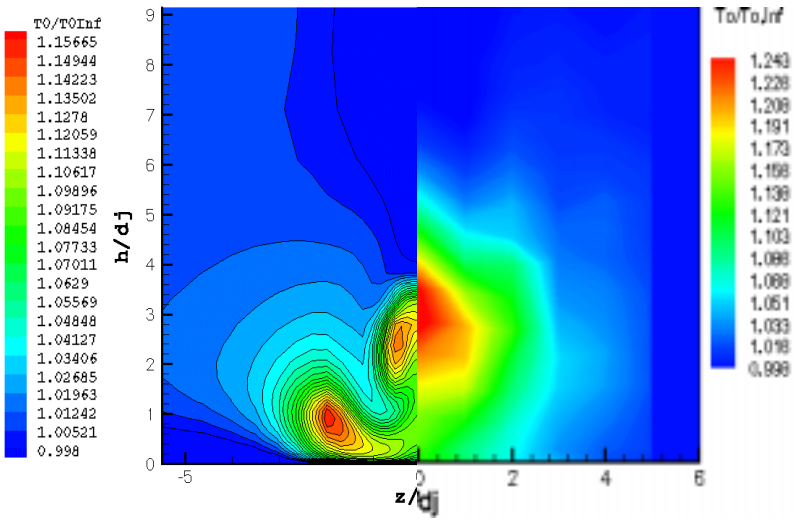


*(b) K-ω turbulence model*

*Figure D.13: Comparison of the contours of the total temperature, 49.8 injector diameters downstream*

The K-ε results look very similar – dimensions, general shape - to the measured total temperature profile, with smoother contours. The CFD model adequately predicts the stoup-shaped profile near the central line of the core. The presence of hot methane along the floor is well captured. The calculated core is smaller and located 8% lower in comparison with the actual one. The maximum temperature predicted by GASP is 1.7% lower than the experimental results. These two observations are consistent with the non-reactive flow simulation – heavier molecules, absence of exothermic combustion process. The K-ω turbulence model predicts an unrealistic total temperature field. The core splits in two distinct zones, one lying along the test section's floor, the other located approximately at the correct height. The maximum total temperature is under predicted by about 7%. The centerline temperature profiles (Figure D.14) offer another means of comparison.

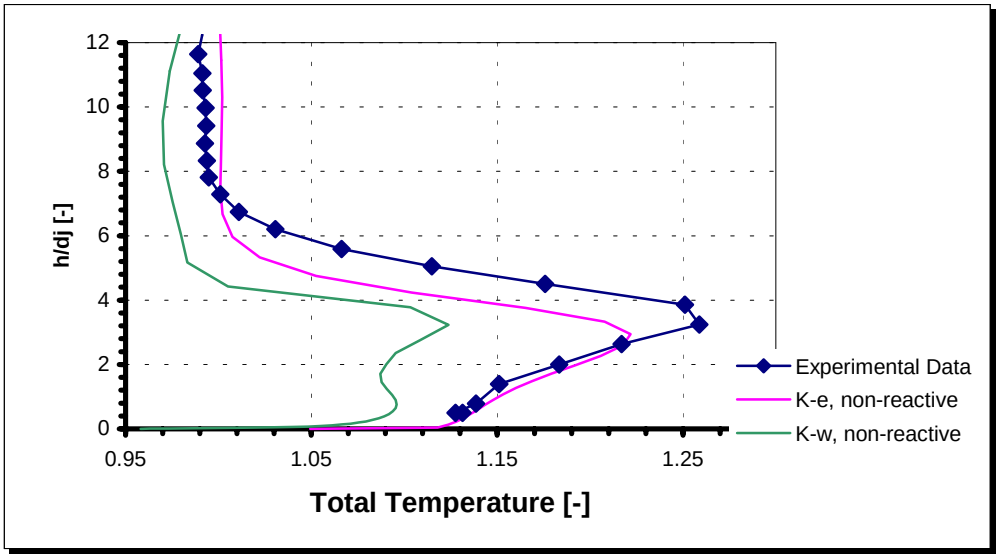


*Figure D.14: Centerline total temperature profile comparison*

The temperature profile predicted by the K-ε turbulence model exhibits a remarkably similar trend to the experimental profile. Both the predicted profile below the maximum temperature ratio and the gradients appear to match the experimental data very well. The results provided by the K-ω turbulence model show poor agreement with the experimental data. The separation of the plume core in two different zones observed in Figure D.15 (b) is confirmed.

*D.3.3.5. Jet Mixing*

Zebra contour plots of the turbulent kinetic energy (Figure D.15 (a) and (b)) evidence the zones of important mixing between the air-stream and the methane jet. The results obtained present significant differences. Nevertheless, the two turbulence models indicate two zones of interest, the first one being located just upstream of the injection port – corresponding to the encounter between the jet and the air-stream -, and the second one downstream of the injection port. The encounter between the air-stream and the methane jet produces a large mixing region for the K-ω turbulence model, while the K-ε model predicts a much less extended region. In the downstream region, the results are in complete discordance. The K-ω model predicts the presence of an important zone of recirculation about 5mm downstream of the injection port, where the K-ε model does not

evidence anything. Also, the K-ε model predicts an important turbulent region just downstream of the injection port, which the K-ω model does not show.

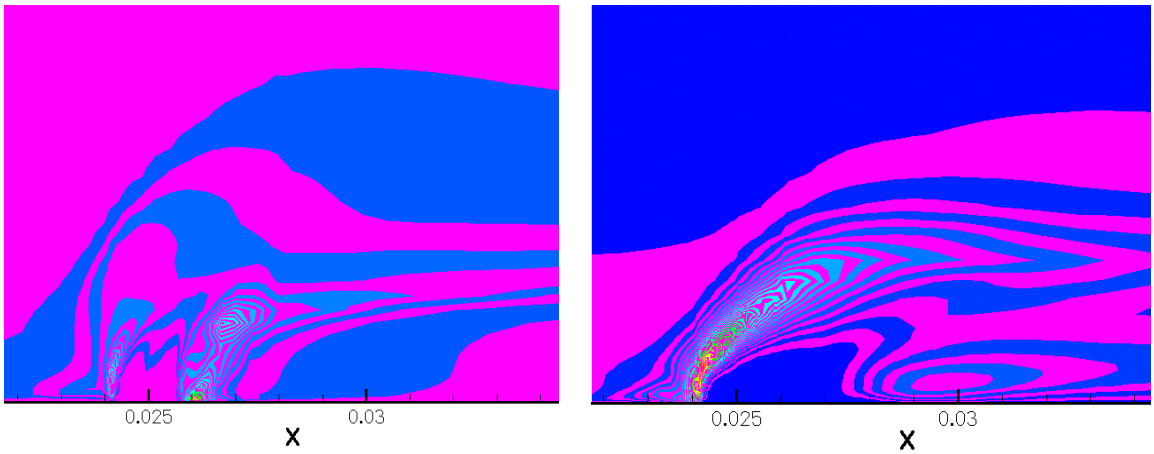


*(a) K-ε Model* *(b) K-ω model*

*Figure D.15: Zebra plot of TKE, evidencing the regions of intense mixing. The injection port is located at x = 0.025 [m].*

*D.3.3.6. Conclusions*

From the results obtained, the following conclusions can be drawn:

❑ The K-ε turbulence model confirms its reputation of numerical stiffness. The numerical solution tends to produce oscillations, making a good level of convergence (3 orders of magnitude or better) challenging. The exact reason for this problem remains unknown. Possible explanations include an inadequate mesh resolution in the injection region, or the use of *walls functions* as boundary conditions.

The K-ω turbulence model, in contrary, presents a very smooth numerical behavior.

❑ Comparison of the solutions regarding initial penetration of the jet evidences some differences between the two turbulence models. The K-ε solution indicates a stronger penetration through the lower portions of the air-stream. The K-ω solution seems not to well represent the penetration characteristics of the jet since the jet does not penetrate the lower layers of the air-stream's boundary layer.

❑ The shock wave structures provided by the two turbulence models are very similar, and match the measured data well. The contours of the mixture density evidence a difference in the evolution rate of the density within the methane jet plume. The K-ε solution shows a rapid increase of the density, and a weak interaction with the test section's floor. The K-ω model predicts a smoother density gradient, and a significantly more important interaction with the wall.

❑ The penetration of the jet plume 49.8 diameters downstream of the injection best highlights the observed differences between the numerical results. The total temperature mapping and centerline profile show good agreement between the K-ε results and the experimental data (FigureD.13 and D.14). The differences observed regarding the height and total temperature are attributed to the lack of a chemical reaction model. In fact, the exothermic oxidation reactions that are present in the real flow increase the temperature of the jet plume. The resulting decomposition of the methane in smaller molecules and radicals lowers the average molecular weight of the flow particles, engendering a higher located and larger plume core than calculated. The K-ω results do not match the experimental data. The predicted jet plume exhibits an unrealistic shape.

❑ Globally, the K-ε turbulence model provides excellent overall results. The accordance with the experimental data, in spite of the crude assumption of negligible effects of the chemical reaction on the flow, is impressive.

❑ The K-ω turbulence model fails to match the experimental results. This is likely the result of the unrealistic eddy – turbulent – viscosity and laminar viscosity ratio necessary to preserve the monotonicity of the numerical solution. The behavior of the initial penetration of the jet and the total temperature mapping downstream seem to indicate a very viscous flow field. It appears that the artificially increased laminar viscosity prevents an accurate representation of the physics of the flow. This shows the potential weakness of all the turbulence models, which are all based on the Boussinesq approximation of the existence of a turbulent viscosity.

## D.4. Reactive Flow Simulation

From the previous section, it appears that the K-ε turbulence model is the best choice for modeling the plasma jet problem and so will be the only model used for the reactive flow simulation.

### D.4.1. Numerical Setup

The computational domain is rigorously identical to that of the non-reactive case. The spatial discretization, however, presents two differences: (1) the number of blocks is reduced from four to three, and (2) the injection area is modeled using a pole domain. Figure D.16 shows a 3D isometric view of the domain. The boundary conditions have not been modified.

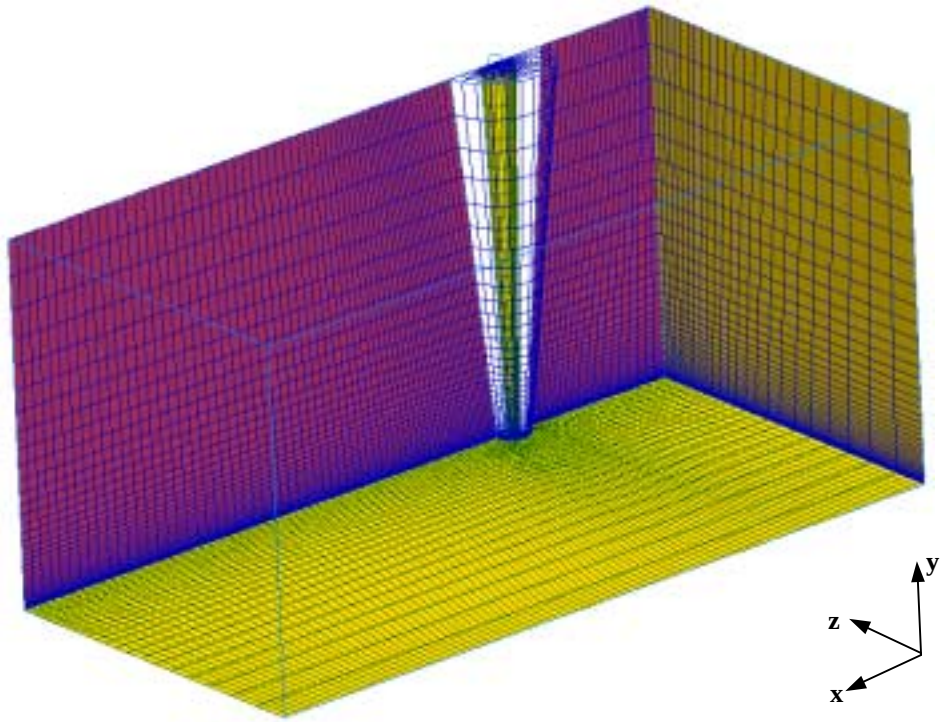


*Figure D.16: Isometric view of the mesh, reactive K-ε case*

FigureD.17 provides a detail of the pole domain that discretizes the injection port region – a structured grid surface that has been collapsed to a line. The pole domain is used for two reasons. First, this design increases the mesh density in the center of the

injector, identified previously as a possible cause for the convergence problems encountered with the non-reactive simulation. Second, it simplifies the writing of the primitive vector **q** necessary to impose the jet inflow conditions thanks to the angular symmetry of the mesh. The number of grid points is decreased of 12% in comparison with the non-reactive case, totalizing 103,680 cells. The numerical setup is identical to that of the non-reactive case, the same convergence-enhancing strategies are chosen.

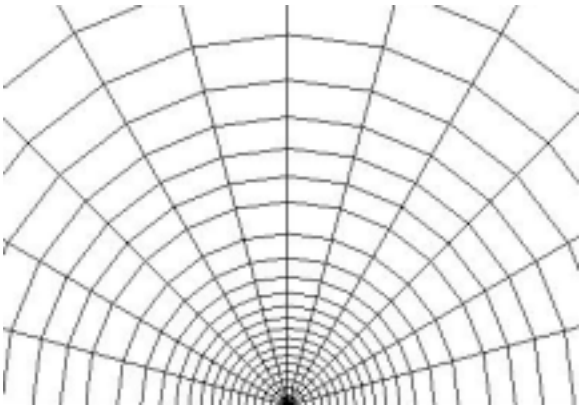

Fig D.17: Structure of the pole domain

**D.4.2. Results and Discussion**

The results are to be evaluated on the basis of: (1) the convergence history, (2) the shock system, and (3) the total temperature mapping and centerline distribution, exactly as done in the previous section for the non-reactive flows.

*D.4.2.1. Convergence history*

Figure D.18 shows the evolution of the normalized residuals throughout the simulation. The four blocks are clearly distinguishable.

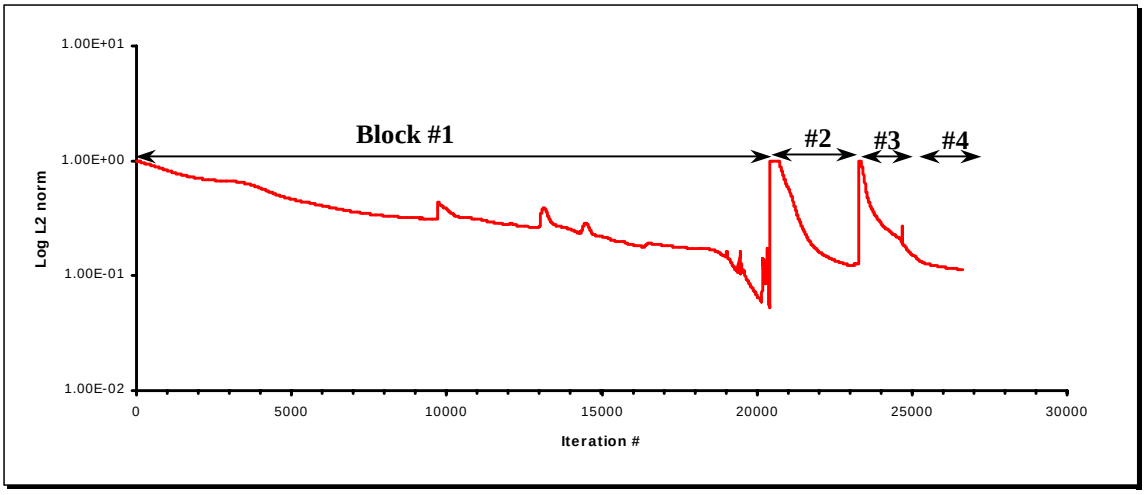


*Figure D.18: Convergence history, reactive-flow, K-ε simulation*

The problem presents an extremely stiff numerical behavior. The monotonicity of the numerical solution is difficult to preserve. The CFL condition must be reduced to extremely restrictive values – down to minus 6 orders of magnitude. This, however, makes sense with the qualitative definition of the CFL number, which stipulates that the physical scales – time, characteristic lengths - must be contained within the numerical scales [9]. Since the characteristic time scale of a chemical reaction is of the order of the μs [10,11], the maximum time steps allowing converging the solution are even smaller. As a consequence, the number of required iterations increases dramatically. More than 20,000 iterations are necessary to reach 1.5 orders of convergence on the coarser grid. The two finer grids are easier to converge, but with a CPU time per iteration of more than 2 minutes on six processors of the SGI *Origin 2000* – 15 minutes of real time – on the finer grid, the total time necessary to reach convergence is prohibitive. The solution is hence considered to have reached its maximum convergence when the residuals stopped to evolve faster than $10^{-5}$ orders per iteration, what happens after 3,000 iterations in the fourth block, and about two weeks of CPU time.

The poor convergence observed is likely to have been caused by the pole zone. A check on the residual outputs reveals this zone to be the most unstable, and the slowest to converge. The contours of the total temperature near the injection port (Figure D.19) confirm an inadequacy of the mapping between the adjacent zones located in that area. The singular axis is also clearly evidenced. The origin of this problem can be either the mesher or the solver. The presence of two faces lying in the same plane cause the pole

domains the to be potentially mathematically inconsistent [12]. In spite of the poorly converged numerical solution, it is worthwhile comparing it with the experimental data to see if the trends of the solution confirm the adequacy of the K-ε turbulence model for modeling the plasma jet injection.

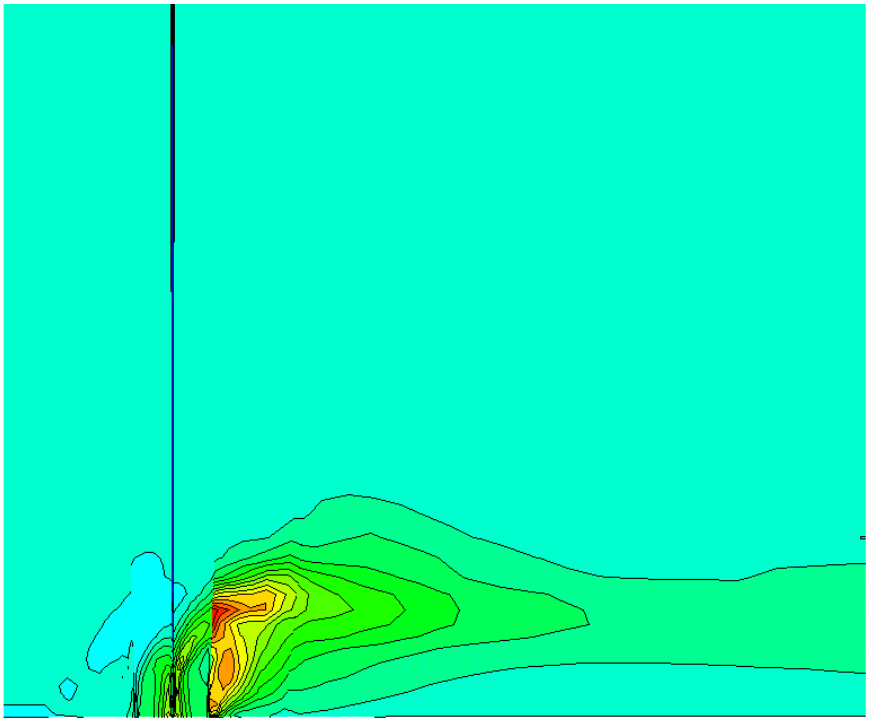

*FigureD.19: Total temperature field, evidencing the singular axis and the bad mapping between the adjacent zones in the injector area.*

*D.4.2.2. Shock System*

Figure D.20 shows the mixture density field obtained from the reactive-flow simulation. Although the aforementioned convergence problem is apparent, the shock structure is clearly identifiable, just ahead of the red/orange areas. The boundary layer edge is located at the transition between the green and yellow regions of the domain. The predicted shock angle – 31° - matches the experimental value measured from the shadowgraph (Figure D.12 (c)).

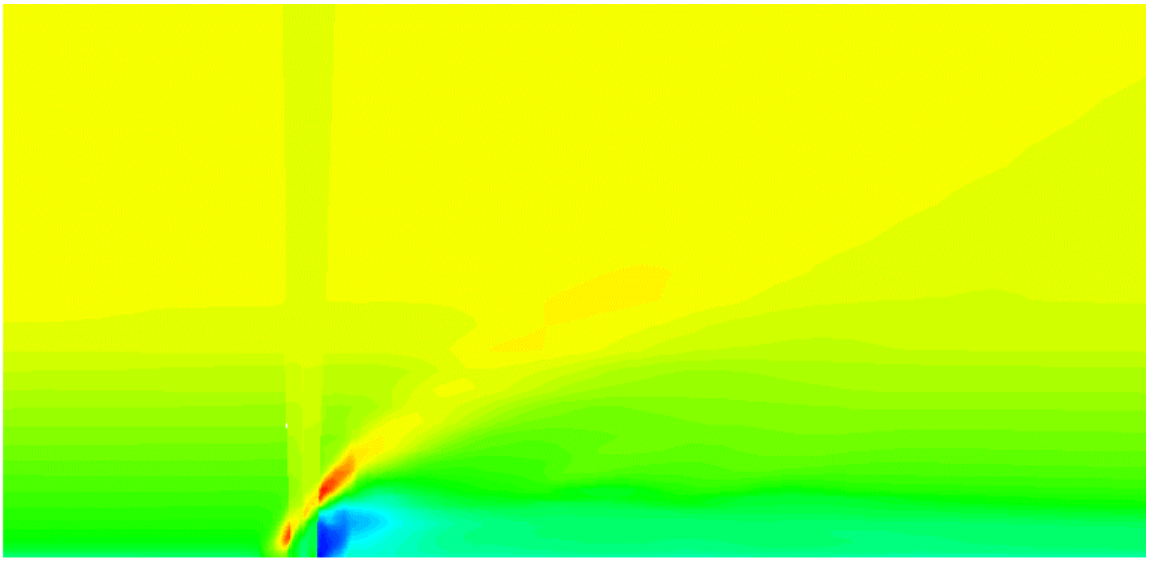

Figure D.20: Mixture density, reactive-flow simulation

*D.4.2.3. Penetration*

The total temperature mapping 49.8 injector diameters downstream of the injection port does not adequately match the experimental data. If the polygonal-shape is about correct, the whole plume looks flattened. The presence of hot gases along the wall is captured, as well as the characteristic stoup-shaped central temperature field. The core is located 1.7 injector diameters, about half the height of the experimental results, and the maximum core temperature is under predicted by almost 10% (Figure D.21).

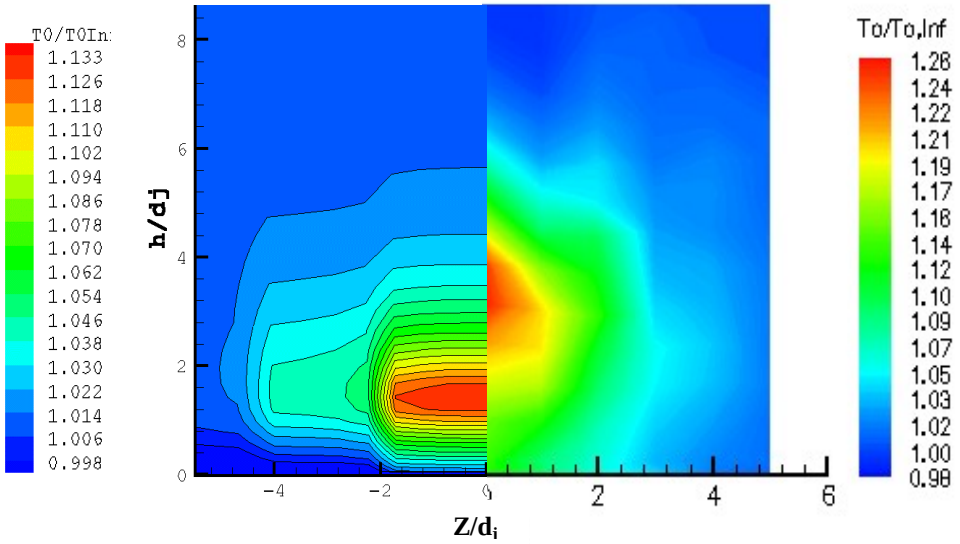


Figure D.21: Comparison of the contours of total temperature, 49.8 injector diameters downstream

Figure D.22 compares the centerline total temperature profiles obtained from the different cases. The poor overall agreement of the reactive-flow simulation with the experimental data is confirmed. If the profile exhibits about the correct shape and the gradient below the maximum core temperature resembles the measured one, the overall result is even less accurate than the prediction made by the non-reactive K-ω simulation.

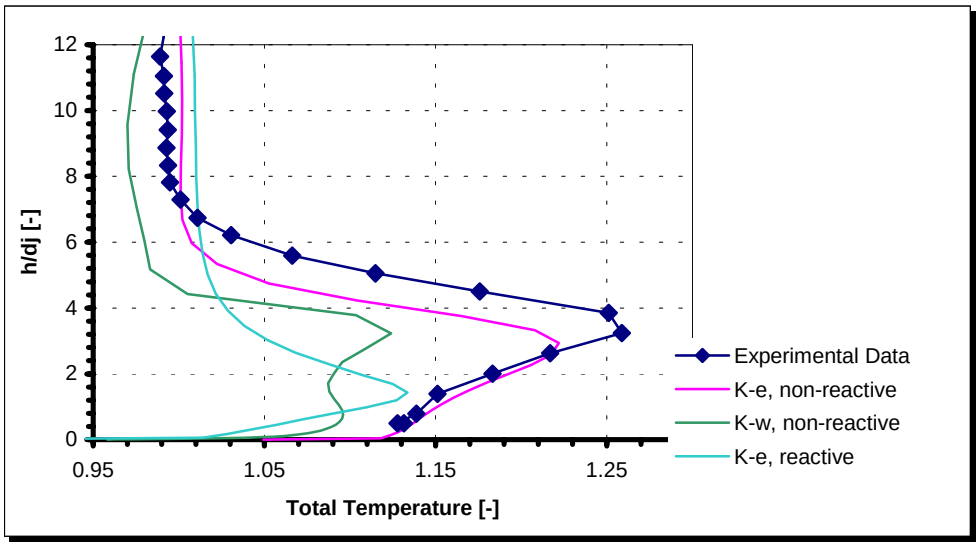


*Figure D.22: Total temperature centerline profile comparison*

### *D.4.2.4. Conclusion*

The K-e turbulence model reveals again a significant numerical stiffness. The convergence of the solution is really difficult. The presence of the chemical model increases dramatically the computational cost, increasing the CPU time by a factor 10 in comparison with the non-reactive case on a comparable grid, and requiring extremely severe CFL criteria. The presence of a pole zone in the spatial discretization worsens the numerical stiffness of the problem. For reasons yet to be explored, GASP could not adequately simulate a complex flow on a grid featuring such a pole zone. In spite of the poor convergence, the shock system is correctly solved. The predicted oblique shock angle matches the measured angle well. The total temperature profile downstream does not match the experimental data. The agreement of the general plume shapes is good, but both the plume core height and temperature are largely under predicted. Finally, the responsibility of the pole zone remains in question.

## D.6. Conclusions and Recommendations

The purpose of the present study was to model a jet of methane gas passing through a plasma torch and injected normal to a supersonic Mach 2.4 cross-flow. The situation corresponds to experiments carried out in Virginia Tech's wind tunnel.

The case involves three physical phenomena: (1) the compressibility of the flow, (2) the viscous and turbulent effects, and (3) the oxidation process of the methane gas. Each represents a difficult problem on its own. Compressible flows are likely to present blunt discontinuities, shock waves, the turbulence models implemented in the codes are often numerically stiff and inaccurate, and the chemical models are expensive in computational cost.

A 3-step pyramidal approach was chosen to model the case. The first step was to simulate a compressible flow over a flat plate, using the Euler equations, and the Navier-Stokes equations – viscous, laminar. This simple case demonstrated GASP's ability to adequately simulate detached shocks and compressible boundary layer in supersonic conditions. The next step was to correctly model the flow conditions prevailing in the test section where the experimental data were collected. Two different turbulence models were tested: (1) a K-ε model, in conjunction with *wall functions,* and (2) the K-ω model, with full integration of the flow equations to the wall surface. Simulations carried out on a flat plate for the K-ε turbulence model, and in a nozzle for the K-ω model, provided results that matched very well with those determined from the measured flow condition within the wind tunnel.

The main step was the simulation of the methane injection. A model for the injection conditions – mass-flow, temperature, pressure, velocity – was derived from the fundamental laws of thermodynamics and heat transfer, using the known measured data – plasma torch topology and power rating, feedstock conditions. An existing 13-specie 11-step chemical model for the oxidation of methane in air was coded in GASP. The chosen model provides an adequate representation of the reaction mechanism given the purpose of this work.

Initially, the plasma jet injection was simulated as a non-reactive flow. This provided an excellent means of comparison between the two turbulence models chosen.

The K-ε model, despite important numerical stiffness causing problematic convergence, produced results in good accordance with the experimental data. The total temperature centerline profile and contours 49.8 injector diameters downstream of the injection port were in very good accordance with the measurements. The K-ω case, albeit easy to converge, did not provide a satisfactory solution and appears to have difficulties modeling jet injection problems. A shortcoming of the turbulence model itself seems to be the origin of the problem. Actually, to preserve the monotonicity of the numerical solution, a modification of the ratio between eddy and laminar viscosities is required. This is likely to have induced a non-physical increase of the flow laminar viscosity that eventually prevented an accurate representation of the physics of the flow.

The last step of the study involved the complete simulation of the reactive plasma jet injection. The computational cost was extremely high – more than ten times that of the non-reactive case – because of the increased number of unknowns and the severe CFL stability conditions required by the chemical model. The presence of a pole zone resulted in a poorly-converged solution, and incomplete resolution of the flow. For this reason, the results did not match the experimental data well. The shock structure was fair, but the total temperature mapping and centerline profile presented an error of 10% for the temperature value and about 50% for the location of the maximum plume core temperature. These results demonstrate that modeling the injection of a plasma jet into a supersonic cross-flow is an achievable goal for a CFD solver like GASP. The model built for the methane jet proved to be accurate enough for the purpose of the study.

More complex cases are certainly within reach. The main concerns are the computational cost, which become rapidly prohibitive, and the numerical stability of the model. An enhancement of the stability would probably imply an increase of the mesh resolution, which in turn would induce an increase of the computational cost – proportional to the number of cells to the cubic power. This dilemma between stability and computational cost shows the limitation of the CFD tools. Even more efficient numerical methods must be fund, and the computer capabilities even improved. The need for better turbulence models has also been highlighted. All the actual turbulence models are based on the Boussinesq assumption of the existence of a turbulent viscosity. Actually any single turbulence model acts by modifying locally the viscosity of the flow.

This adequately works for trivial situations, but is largely insufficient when the flow is highly three-dimensional [13]. New turbulence models based on statistical methods and/or the direct resolution of the Reynolds turbulent transport formulations would be desirable.

To improve the accuracy and usefulness of the model, the first step would certainly be to rerun the reactive K-ε simulation using an improved mesh and allowing the solution to converge very slowly, using small time steps, even if that implies months of computations. The K-ε turbulence model should be tested without *wall functions*, which were identified as a possible cause for the poor level of convergence observed. A second step would be to seek other ways to improve the convergence speed, maybe trying other combustion models for the methane. A campaign of experimental measurement of the exact chemical evolution of the reaction would help finding the right chemical model. Once a reasonable model is correctly set for the 1500W plasma torch, other configurations should be tested to validate the model. If the model still holds, the doors are open to tackle more realistic configurations, and/or generalize the model for other feedstock gases.

## D.6. References


[1] Borel, L., Thermodynamique et Energétique, vol.1, Presses polytechniques et Unviversitaires Romandes, Lausanne, 1987

[2] Gallimore, S.D., Operation of a High Pressure Uncooled Plasma Torch with Hydrocarbon Feedstocks, MS Thesis, Virginia Polytechnic Institute and State University, Blacksburg, Virginia, 1999

[3] Moran M.J., Shapiro, H.N., Fundamentals of Engineering Thermodynamics, 2nd Edition, Wiley & Sons Inc., New York, 1992

[4] Incropera, F.P., DeWitt, D.P., Fundamentals of Heat and Mass Transfer, 4th Edition, Wiley & Sons Inc., New York, 1996

[5] Kato, R., Kimura, I., Numerical Simulation of Flame-Stabilization and Combustion Promotion by Plasma Jets in Supersonic Air-Streams, 26th International Symposium on Combustion, The Combustion Institute, 1996

[6] Schetz, J.A., Cox-Stuffer, S., Fuller, R., Integrated CFD and Experimental Studies of a Complex Injectors in Supersonic Flows, 20th AIAA Advanced Measurement and Ground Testing Technology Conference, June 15-18 1998, Albuquerque, New Mexico

[7] Bowman, C.T., Seery, D.J., Investigation of NO Formation in Combustion Processes: The Methane-Oxygen-Nitrogen Reaction, *in* Proceedings of the Symposium on Emissions from Continuous Combustion Systems, General Motors Research Laboratories, Plenum Press, New York, 1972

[8] Edelman, R.B., Harsha, P.T., Laminar and Turbulent Gas Dynamic in Combustors – Current Status, *in* Progress in Energy and Combustion Sciences, vol.4, Pergamon Press, Oxford, 1978

[9] Drotz, A., Mécanique Numérique des Fluides Incompressibles, notes de cours, Ecole Poytechnique Fédérale de Lausanne, DGM-LMH, Lausanne, 1999

[10] Hill, P., Peterson, C., Mechanics and Thermodynamics of Propulsion, 2nd Edition, Addison-Wesley Publishing CO, Reading, Massachusetts, 1992

[11] Lefebvre, A.H., Gas Turbine Combustion, McGraw Hill, New York, 1983

[12] Collective, Gridgen version 13.3 User's Manual, Pointwise Inc., Bedford, Texas, 1999

[13] AGARD-AR-355, CFD Validation for Propulsion System Components, edited by Dunham, J., Neuill-sur-Seine, May 1998

## *Vita*

Scott Gallimore was born in Sacramento, California, May 14, 1975. His family traveled to Germany, Colorado and eventually Northern Virginia. Scott graduated from Lake Braddock Secondary School in 1993, with honors, and attended Virginia Tech in the fall of that same year. He had several internships between semesters; working for a local organization as a tennis instructor, an AutoCAD engineer for American Systems Corporation and an engineering assistant for General Motors. Scott earned his B.S. degree, magna cum laude, in Mechanical Engineering during the spring of 1997, followed by his master's in August of 1998.

Continuing the work of his master's project, Scott enrolled as a Cunningham Fellow August of 1998 as a doctoral student. Through his three-year doctoral work, he received multiple awards including the Gordon C. Oates Airbreathing Propulsion Award, a national award given by AIAA to one outstanding doctoral student per year. Scott also received excellent student feedback as an instructor, receiving high marks on his teaching evaluations.

Upon graduation, Scott plans on entering the hypersonics field, developing scramjet engines for high-speed vehicles.